Stony Brook University

The official electronic file of this thesis or dissertation is maintained by the University Libraries on behalf of The Graduate School at Stony Brook University.

Stony Brook University

Optimization of CIPS based Opto-electronic gas detectors.

Methane detector.

A dissertation Presented

By

William Cheng

To

The Graduate School

in Partial Fulfillment of the

Requirements

for the Degree of

Doctor of Philosophy

in

Electrical Engineering

Stony Brook University

December 2016

Stony Brook University
The Graduate School

William Cheng

We, the dissertation committee for the above candidate for the
Doctor of Philosophy degree, hereby recommend
acceptance of this dissertation.

Mikhail Gouzman– Dissertation Advisor
Adjunct Professor, Department of Electrical and Computer Engineering

Milutin Stanacevic - Chairperson of Defense
Associate Professor, Department of Electrical and Computer Engineering

David Westerfeld
Assistant Professor, Department of Electrical and Computer Engineering

Michael Gurvitch
Professor, Department of Physics and Astronomy

This dissertation is accepted by the Graduate School

Charles Taber
Dean of the Graduate School

Abstract of the Dissertation
Optimization of CIPS based Opto-electronic gas detectors.

Methane detector.

by
William Cheng
Doctor of Philosophy
in
Electrical Engineering
Stony Brook University
2016

The infrared molecular absorption spectra of certain gases are used for the spectroscopic detection of the presence or concentration of gas. Various and unique techniques utilizing this spectrum have been employed to improve detection, each with its own merits. CIPS (Correlated interference polarization spectroscopy) is unique in how it provides high sensitivity along with high selectivity. The work presented builds on the achievements of CIPS as it was developed by BAH Holdings and its members.

This Dissertation reports on modelling of CIPS and its constituents such as the electro-optical modulator. The development of the generator used in this system was also described. The mathematical model of the correlated interference polarization filter (cIPF), modulator, and etalon was derived and the parameters optimized. The optical response of the CIPS mathematical model to methane was presented. Several experiments were carried out to support the model and characterize critical properties of the modulator. A smart generator which drives the modulator was redesigned to be more efficient, robust and lower cost.

Our work furthers the improvement of CIPS technology, in particular its limitations and potentials, and provides a framework for further studies and development specifically in two directions. It was shown that COMSOL can be used to develop new modulator designs. The technique for detection of other gases besides methane can utilize the same mathematical modeling framework.

Table of Contents

List of Figures

List of Tables

Acknowledgments

I would like to express my gratitude towards my advisor and close mentors Michael Gouzman and Michael Tkachuk, without whose guidance and support I could not have completed this work.

I would also wish to thank the following people:

Dr. Alex Shabolov for his encouragements and for help in construction of experimental equipment.

The people of SensorCAT and my colleagues, new and old, for their company and friendship and for providing me with valuable knowledge and suggestions.

Last but not least my family and Yi Chun Ma for their constraint motivation and loving support.

Chapter 1 Introduction

Gas sensing is extensively used both in and off our world. Much effort and energy has been expended to expand this field as evident in the wide variety of gas sensors and gas sensing techniques. This dissertation mainly focuses on the optical detection of methane and hydrocarbon gases and presents the results of research done to this effect. The main objective of the research was to analyze and improve by redesign, the elements of the methane sensor.

This dissertation begins with an introduction on the types of gas sensors, followed by an explanation of correlated interference polarization spectrometry (CIPS). The optical structure of CIPS and some of its constituents is analyzed. Work done on the photoelastic modulator (PEM), a component in CIPS, is then presented. The last section covers work on the generator which provides the electrical power as well as maintaining resonance of the modulator.

Methane sensing is an important tool in many different fields of science as methane is ubiquitous. Liquid natural gas (LNG) is mainly composed of CH_4 and has been growing in use as an alternative fuel. LGN is typically extracted from the ground, refined and piped or trucked to be used. However, methane in concentrations higher than 4.4% has the potential to combust or explode and even higher concentrations will cause asphyxiation. The development of methane gas leak detectors is then crucial to provide a useful tool to detect faulty natural gas pipes. Methane is also a greenhouse gas; the second most prevalent greenhouse gas after carbon dioxide. It is also a product of anaerobic respiration a process in which microorganisms living in landfills, ruminates and humans break down organic compounds for respiration. In our case we are cooperating with BAH to make and improve upon a sensor that can detect methane up to 100 ppm with a resolution of 1 ppm or so. This is used in Bedfont's Gastroch4ek[1], a

machine for the medical profession to help diagnose irritable bowel syndrome which is assumed to be an imbalance in microscopic gut flora. In this case, sugars which are not digested before reaching the large intestines are processed by microbes and eventually become methane which gets absorbed into the bloodstream. The methane is then transported to the lungs by blood and expelled through the breath by the process of respiration as the gas diffuses through the blood-air barrier.[2]

1.1   Physical principles of optical gas detection

Hydrocarbon detection systems extend to a broad range of sensor types. A good starting place is to categorize the systems to two families which we will term physical sensing and remote sensing, both types are based on physical interactions with the hydrocarbon gas, the first interacts with a material which changes its property, while the second measures the change of the interaction. A further classification would be to define them based on its principal of its operation mechanism. We will provide a brief overview of some detectors.[3]

Physical sensing:

Electrochemical- Operates by oxidizing or reducing the gas at a sensing electrode and measuring current or voltage, it is sensitive up to the PPM range. This of course requires a direct interaction of the gas and hence the gas must be electrochemically active. This type of sensor can also be sensitive to other gases which must be taken into account during its design. The output can drift over time and operating life is in the order of several years. [4]

Solid-State Conductivity- Measures the resistance change due to the presence of a gas near a heated surface of metal oxide. This type of sensor responds to an even larger range of gases than electrochemical sensors (poor selectivity). The sensors also suffer from drift and are sensitive to humidity and temperature, but they have an operating lifetime longer than electrochemical sensors.[5, 6]

Photo-Ionization (PID) Gas – operates by ionizing volatile organic compounds with ultraviolet light; the number of ions counted corresponds to the concentration of gas. Its

sensitivity ranges from ppb to ppm. The detector again cannot be made to be sensitive to only one type of gas. Its response is also heavily dependent on humidity, and can be quenched by large concentrations of a gas such as methane or water vapor due to the high ionization potentials of those gases that are required to produce ion current.[7]

Flame-Ionization (FID) - Is similar to PID, with the source of ionization substituted with a hydrogen flame. This is very effective for the detection of hydrocarbons due to the presence of carbon, but it requires a large setup with tanks of compressed hydrogen.[8, 9]

Colormetric – Uses a chemical coating that changes color when exposed to a particular gas. This type of sensor is cheap and can be used as simple indicator of exposure or presence of a gas. The process is typically nonreversible, and thus is used as a one-time indicator.[10]

Catalytic Bead - Fine platinum wire is used in conjunction with a catalyst to promote oxidation of gas. The presence of gas causes oxidation and the reaction raises the temperature at the catalyst, which can be detected though a Wheatstone bridge. Because it is an oxidation reaction, the presence of oxygen then is necessary for detection.[11, 12]

Optical sensors:

Optical sensors operate by measuring the interaction of the gas with the electromagnetic spectrum. All optical sensors rely on the Beer-Lambert law (1-1) to some extent, which dictates the attenuation of light to the properties of the material it passes through. CIPS sensors fall under this category.

$$I_{out}(\lambda) = I_0 e^{-\alpha(\lambda)CL} \tag{1-1}$$

Tunable Diode Laser Absorption Spectroscopy (TDLAS)-

A tunable diode laser's emission spectrum is swept over an absorption line in the gas spectrum and the intensity of light is measured. The change in signal is small over a large background however and noise is a large factor. Sensitivity of single pass direct absorption spectrometry or DAS is limited to an absorbance of 10^-3, and the diodes are

3

expensive to produce. However this style of sensor applying other techniques such as Modulation and cavity-enhanced absorption spectrometry (CEAS) is capable of higher sensitivity.[13-15]

NDIR-

NDIR or Non-dispersive Infrared gas sensors are sensors that use spectroscopy to detect concentration of particular gas molecules. The NDIR sensor's design can be broken up into four main sections; an IR source, a chamber that can contain the gas under study, a filter, and an IR detector.[16] It is called non-dispersive due to the fact that the light spectrum is not spatially separated throughout the whole light path nor is it filtered by polarizers. The system instead relies on the difference in intensity of light passing through a sample. The NDIR then needs a reference signal for zero concentration of gas. It also benefits from also knowing the intensity of light which passes through the highest concentration of gas or the lowest intensity of light. This helps with stability as the components of the sensor degrade and change over time. The IR source as it ages, changes not only the intensity of IR light but also the spectral curve. Currently the system is very mechanical, as different chambers containing samples of gas are rotated into and out of the path of light.[4] This is one of its major disadvantages as a moving field of view and mechanical operation imposes a limit on its sensitivity and lifetime. New advances in mid IR LED technology however are opening up possibilities for smaller and more stable sensors.[17]

Chapter 2 CIPS

CIPS is a hydrocarbon gas detection system, in the context as described in this dissertation; it is designed to detect methane gas CH_4 with several clear advantages to other systems in the market. It has lower power consumption and is much more robust due to a lack of physically moving parts compared to other nonphysical measurement systems. CIPS is designed to have high sensitivity (0.5 ppm) and high selectivity. The intensity of light is compared to baseline intensity through a shift in the center frequency of a comb filter.

2.1 Methane IR spectrum

The IR spectrum of methane is due to its vibrational modes. The tetrahedral molecular structure of methane gives rise to asymmetric vibrational modes which corresponds to spectral lines; symmetrical vibrational modes do not produce IR as they are not associated with any changes in the dipole moment. Methane is a symmetric top molecule with no net dipole moment until it is excited into certain vibrationally excited states. A spherical top molecule has three equal moments of inertia.[18] In reality, the ideal spectral lines corresponding to the vibrational modes are spread out or broadened. Spectral broadening sources include pressure and temperature.
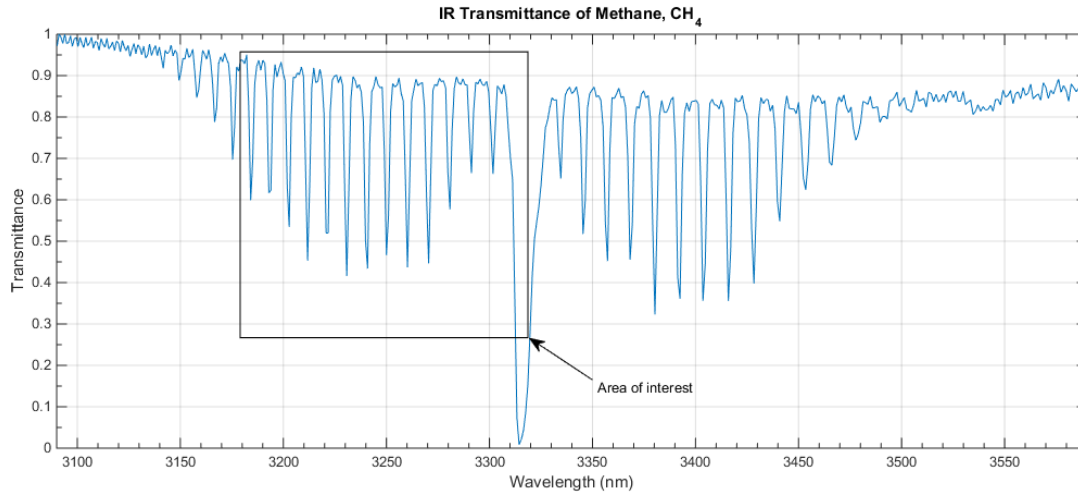
Figure 2-1: Methane transmission spectrum. Most hydrocarbons exhibit a response to IR light, absorbing wavelengths of light associated with the molecule's vibrational/rotational modes. (Spectrum provided by Dr. Michael Tkachuk)

One of the causes of spectral broadening is the constant motion of molecules of gas. The velocity of the individual molecules of gas then shifts the spectrum due to the Doppler Effect which then causes the spectrum to broaden in an inhomogeneous manner. The shape of the Doppler broadening is Gaussian due to the Gaussian distribution of the gas velocities with respect to a stationary sensor. As temperature is a measure of the molecular kinetic energy, it dictates the velocity of the molecules and thus ultimately the spread (or variance:σ^2) of spectral lines.

Pressure also affects the oscillations of the dipoles. The molecular oscillations give rise to the spectral shape with each peak corresponding to a different vibrational mode. Pressure has an effect on the collisions between molecules by acting as the dampening experienced by the molecules. Collision broadening then widens the spectral lines with a Lorentzian line shape due to its association with dampening on resonance.[19]

Opacity broadening is another effect which occurs in a special condition where the gas emission spectrum gets reabsorbed by the same type of gas at a lower temperature. The result is that the emission spectrum which is wider due to thermal

Doppler shifts has been reabsorbed by the cooler section of gas with the absorption spectrum narrower but still centered at the same spectral lines.

2.2 CIPS Overview

CIPS technology was developed by Michael Tkachuk, Valeri Alexey Novikov, and Constantine Dean Capetanopoulos in BAH Holdings LLC and Ecolotrol with a series of patents issued from 2001 onwards.[20-23] From the author's limited research the only other source for the development were references to PIFs (polarization interference filters) correlated and otherwise, and to "The Technique and Practice of Spectroscopy" [24] written in Russian. The acronym CIPS is described and explained in the following:

2.2.1 Correlated

Correlated here is in reference to the relationship between the light flux of the device when the cIPF filter's moving spectrum corresponds with the methane spectrum. Typically in a MMSD (modulated mask single detector) gas filter, positive correlation is described as the absorption of light in the presence of the target gas S_{gc} when it is compared to a clear cell S_{cc}. The correlation signal is $\Delta S = S_{gc} - S_{cc}$ A negative correlation exists when the gas is 'hot' and radiates in the emission lines. The result is a decrease in ΔS for increasing concentrations of gas. In CIPS, ΔS is calculated from the signal when the filter is aligned to the methane spectral lines or peaks as the reference signal S_p as compared to the signal when the filter is aligned between the spectral lines or the valleys S_v.

$$\Delta S = S_p - S_v \tag{2-1}$$

Here ΔS grows due the decrease in S_v for larger concentrations of methane gas and thus is positively correlated. It can also be inferred that in the case of 'hot' methane the correlation would switch to negative correlation as S_v would grow for larger concentrations of methane.

2.2.2 Interference polarization

A critical component in CIPS/cIPF is the polarizing interference filter. This device has its origin in France and was first developed by B. Lyot hence its alternative name

'Lyot Filter'. The original invention composed of stacks of birefringent plates with polarizing filters oriented at 45° to the optical axis of the plates. Each subsequent layer has a plate whose thickness is double the previous.[25, 26] These stages filter out light through the transmissions of the individual stages with the result of only passing wavelengths of light that is an integer multiple of the path lengths of all stages. In reality however, we are only using a single stage of the lyot filter resulting in a spectral transmission similar to what is seen in Figure 2-2 as stage 6, and are taking advantage of the manner in which it operates via polarized light. The wave-plate stage is then replaced by a photoelastic modulator and etalon which are still sandwiched between two polarizers.
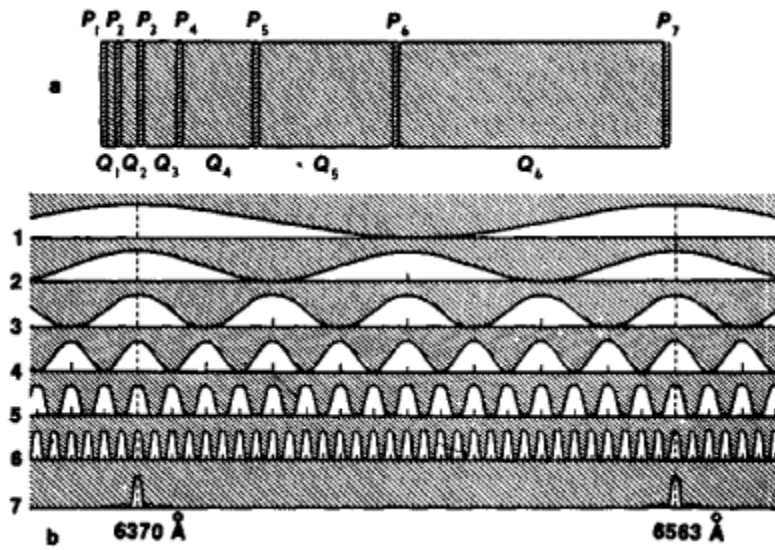
Figure 2-2: (a) Diagram of a polarizing interference filter: (P) polaroid filters, (Q) quartz plates; (b) transmission of individual stages (1–6) and of entire filter (7). Wavelengths are shown at bottom. (Figure from [27])

2.2.3 Spectrometer

A spectrometer measures light over a spectrum of wavelengths. The device does not strictly meet the requirements for a spectrometer but instead follows the naming convention first established at Barringer Research Limited.[28, 29] In general, it is accepted that the instrument performs spectroscopy in the sense that it performs spectral recognition by signal correlation.[30-34] The intensity signature corresponds to

particular gases. The cIPF is built such that it is sensitive to only methane gas with very high selectivity, rejecting the effects of the presence of other gases.

2.3   CIPS technical detail

Since CIPS interacts with gas optically, it does not consume/change the sampled gas or degrade the measuring device through interactions with the samples of gas. As an optical system however it does rely on the interaction length through the Beer-Lambert Law and therefore has limited dynamic range. However since CIPS operates over several spectral lines of which has varying amounts of absorption and it's signal is dependent on the integrated spectrum over several spectral lines, its response is nonlinear. Certain spectral lines may saturate on its absorption while other lines still have not in higher concentrations, this means that CIPS will be sensitive on low concentrations of methane from the stronger absorption lines while having a wider dynamic range compared to optical sensors based on a single absorption line due to weaker absorption lines that the sensor then can still detect. Its advantage over NDIR sensors is in its lack of gas cells. The gas cells are expensive to produce and will eventually leak gas. In addition a rotating cylinder is used to swap the gas cells into the light path; the mechanical system thus has a limited lifetime. Mechanically changing the cells limits the maximum detectivity due to the fact that there will always be misalignment or changes in path length despite any advances in manufacturing. Literature on NDIR shows that it was accurate to +/- 25 ppm averaged within 0.1 seconds for CO_2.[4] Our system has higher sensitivity, with the ability to detect 1 ppm.

In more detail, a broad band source of radiation is first filtered in narrow band IR wavelengths and then filtered to -45° polarized light. This light passes through the sample cell (which may contain an unknown concentration of methane). At this point the light spectrum contains the unique signature of the methane absorption spectrum. The optical path then leads to the PEM which is composed of the resonator (a block of piezoelectric quartz crystal) bonded to another block of stress birefringent fused silica crystal. The piezoelectric resonator stresses the fused silica twisting the light to a

circular polarization in a right and left handed manner depending on if the silica undergoes compression or tension as it does in a photo-elastic material at the PEM resonance frequency. The light then passes through a single stage lyot filer that is tuned so that the combs are spaced with the same width as the absorption lines of the methane gas. A lyot filter achieves this by only having light with particular wavelengths selected by its phase delay pass through the filter, light at other frequencies will be absorbed. The resonator functions as to sweep the filter so that it aligns with and then against, the absorption lines of methane with the PEM resonance frequency. The light is then detected by a photo-detector. Since the light flux moves in time as the filter moves at the same frequency as the PEM drive (also known as the reference signal) frequency, the signal from the photo-detector, generated by the light flux, can then be demodulated by a lock-in amplifier which correlates the light flux signal to the PEM reference signal. The use of PEM has the advantages of shifting the signal out of potentially higher noise regions (1/f noise) as well as allowing for the use of a lock-in amplifier which further makes the CIPS device insensitive to noise.

CIPS had several minor problems when sensorCAT was contracted. The problems were characterized and divided among some of the members in our lab. I've been tasked with characterizing and making improvements on the PEM, as well as several other minor tasks which will not be described in this dissertation. The photoelastic modulator is an anisotropic stress birefringent based system that twists light into right handed and left handed circularly polarized light. The stress induced birefringent quartz is bonded to piezoelectric quartz and is driven electronically by a 'generator'.

A Piezoelectric Quartz driver is used to generate the stress/strain in the FS, the primary reason behind using a quartz system is its high quality factor, which when coupled to the high quality of the FS makes the system more efficient in converting electrical energy into transforming linearly polarized light into circularly polarizing light.

The quartz resonates at 67.95 kHz and of course the Q factor of the PEM depends on matching the resonant frequency of the FS to the quartz. Q factor plays a

role in the efficiency of the system transforming electrical energy to mechanical energy and finally to changing the polarization of light.

The cIPF 'generator' was not terribly reliable, sometimes failing to start oscillations, or failing to switch to feedback mode for self-oscillations. This may be due to PEM variances, aging etc. The generator powers and drives the PEM at its resonant frequency via the piezoelectric quartz.

Chapter 3 Optical structure of CIPS detector
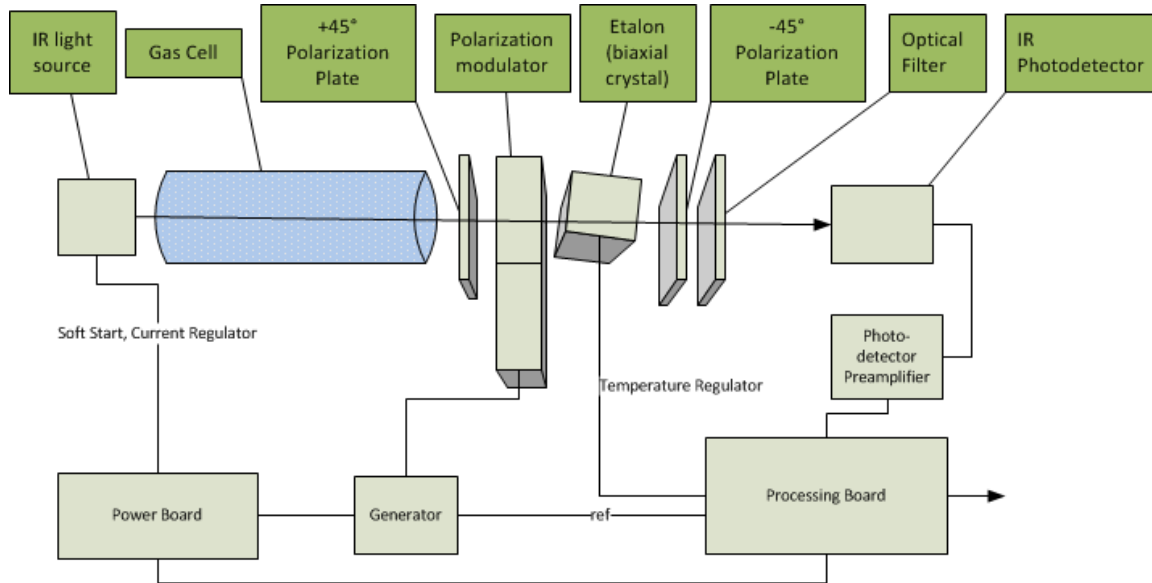
Figure 3-1: CIPS Structure
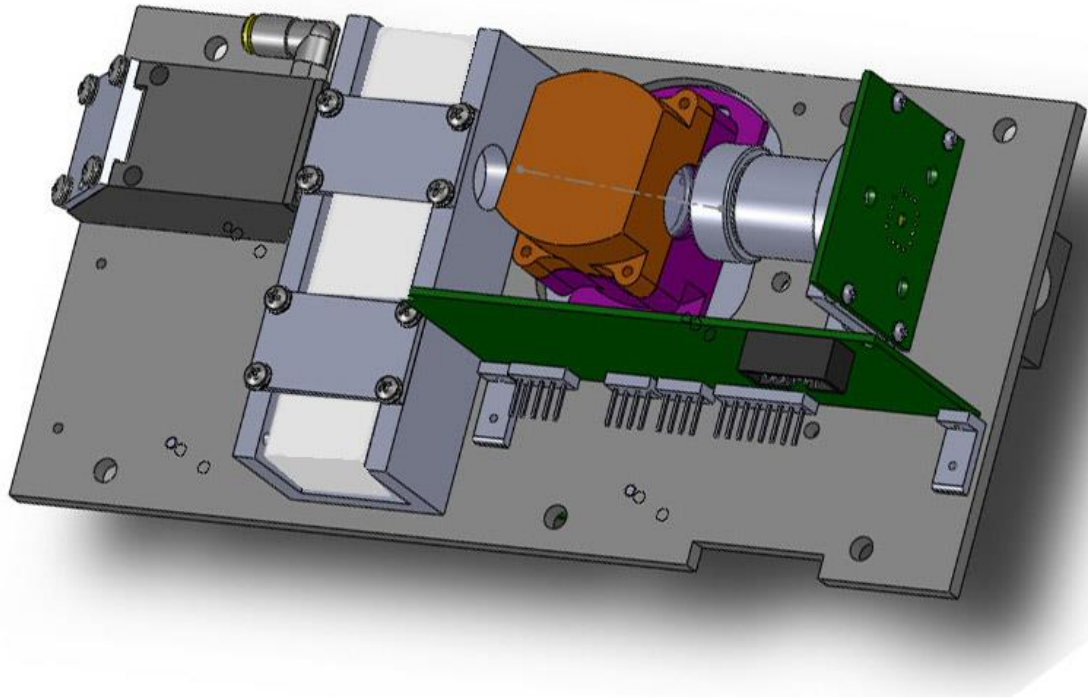
We utilize an incandescent halogen bulb as a grey body IR source which is then pass-band filtered, as our light source. The emissivity of the materials used in its construction, quartz and tungsten are around 0.93 and 0.04 respectively. Factors that affect the output spectrum include operating temperature and aging.[4] The incandescent bulb spectrum shifts over time as a function of aging. Finally the filament sags and changes thickness as it slowly evaporates and redeposits which changes the light beam shape and density. Fortunately the CIPS device is less affected by these changes by its nature of operation: the reference wavelengths of light are located close to the measured peak locations.

3.1 Modulator optical analysis

The PEM acts as a retarder or wave plate which alters the polarization state of the light that passes through it. The phase shift is a function of the birefringence which changes as the FS undergoes compression and tension. In order to understand the

principal of operation and to set the proper amount of modulation we need to use a setup. We also need to describe the PEM setup in mathematical terms.

Our setup consists of the un-polarized light source, band pass filter, linear polarizer, PEM, quarter wave plate, analyzer, and photo-detector. The linear polarizer and analyzer are at 90° to one another. The PEM and quarter wave plate is then introduced between the polarizers and the quarter wave plate's fast axis is oriented 45° from linear polarizer so that the light has a phase shift of $\frac{\pi}{2}$. The PEM can then be tested with the generator which supplies a controlled AC voltage.

The PEM operates by compressing and stretching a fused silica crystal, the stress directed in the horizontal direction gives the crystal birefringency so that the wave passing thorough both PEM and quarter wave plate has either zero degree polarization change or a ±90° change in polarization. The PEM function is represented here using Jones calculus description, where each element is represented by Jones matrices. [35] It is useful to note here that the mathematical analysis shown below is for light of a single wavelength.

Optical, Jones matrix analysis of CIPS Modulator

$$Linear\ polarizer\ at\ 45°: \frac{1}{2}\begin{bmatrix} 1 & 1 \\ 1 & 1 \end{bmatrix}, \tag{3-1}$$

$$Linear\ polarizer\ at-45°: \frac{1}{2}\begin{bmatrix} 1 & -1 \\ -1 & 1 \end{bmatrix}, \tag{3-2}$$

$$Quarter\ wave\ plate, fast\ axis\ vertical, (non\ symetric): \begin{bmatrix} 1 & 0 \\ 0 & -i \end{bmatrix} \tag{3-3}$$

$$linearly\ polarized\ light\ at\ 45° \tag{3-4}$$
$$(L+45)\ is\ then\ represented\ as: \frac{1}{\sqrt{2}}\begin{bmatrix} 1 \\ 1 \end{bmatrix}$$

$$\text{birefringent material (phase retarder):} \quad \text{(3-5)}$$

$$\begin{bmatrix} e^{i\phi_x}\cos^2\theta + e^{i\phi_y}\sin^2\theta & \left(e^{i\phi_x} - e^{i\phi_y}\right)\cos\theta\sin\theta \\ \left(e^{i\phi_x} - e^{i\phi_y}\right)\cos\theta\sin\theta & e^{i\phi_x}\sin^2\theta + e^{i\phi_y}\cos^2\theta \end{bmatrix}$$

Where ϕ_x and ϕ_y are the phases of the electric field in the x and y direction, and θ is the orientation of the fast axis.

At $\theta = 90°$, the birefringent material's fast axis is vertical, so the diagonal terms are zero:

$$\begin{bmatrix} e^{i\phi_y} & 0 \\ 0 & e^{i\phi_x} \end{bmatrix} \quad \text{(3-6)}$$

The phase in the y direction is zero as stress is applied only in the x direction; the stress then changes the electric field phase in the x direction.

Then the birefringent material can be described as:

$$\begin{bmatrix} 1 & 0 \\ 0 & e^{i\phi_x} \end{bmatrix} \quad \text{(3-7)}$$

And the setup can be described with the following:

<table>
<tr><td>-45°linear analyzer</td><td>quarter wave plate</td><td>PEM</td><td>45° polarized light</td></tr>
</table>

$$\frac{1}{2}\begin{bmatrix} 1 & -1 \\ -1 & 1 \end{bmatrix} \cdot \begin{bmatrix} 1 & 0 \\ 0 & -i \end{bmatrix} \cdot \begin{bmatrix} 1 & 0 \\ 0 & e^{i\phi_x} \end{bmatrix} \cdot \frac{1}{\sqrt{2}}\begin{bmatrix} 1 \\ 1 \end{bmatrix} \quad \text{(3-8)}$$

$$\frac{1}{2}\begin{bmatrix} 1 & -1 \\ -1 & 1 \end{bmatrix} \cdot \begin{bmatrix} 1 & 0 \\ 0 & -i \end{bmatrix} \cdot \frac{1}{\sqrt{2}}\begin{bmatrix} 1 \\ e^{i\phi_x} \end{bmatrix} \quad \text{(3-9)}$$

$$\frac{1}{2}\begin{bmatrix} 1 & -1 \\ -1 & 1 \end{bmatrix} \cdot \frac{1}{\sqrt{2}}\begin{bmatrix} 1 \\ -ie^{i\phi_x} \end{bmatrix} \quad \text{(3-10)}$$

$$\frac{1}{2\sqrt{2}}\begin{bmatrix} 1 + ie^{i\phi_x} \\ -1 - ie^{i\phi_x} \end{bmatrix} \quad \text{(3-11)}$$

$$\frac{1}{2\sqrt{2}} \left(1 + ie^{i\phi_x}\right) \begin{bmatrix} 1 \\ -1 \end{bmatrix} \qquad \text{(3-12)}$$

Our PEM operates by stressing the fused silica plate and changing ϕ_x which also changes circularity ϕ. Since the PEM should act as a quarter wave plate, retarding linearly polarized light into either a right hand or left hand circularly polarized light, we assume that the stress changes ϕ from $\frac{\pi}{2}$ to $-\frac{\pi}{2}$ as the PEM compresses and stretches.

$$\frac{1}{2\sqrt{2}} \left(1 - \sin(\phi_x) + i \cos(\phi_x)\right) \begin{bmatrix} 1 \\ -1 \end{bmatrix} \qquad \text{(3-13)}$$

For simulating the signal ϕ_x, the input is of the form $A\cos x$, this describes the stress in the FS from the AC drive on the PEM.

The PEM's ϕ_x is a function of stress on the fused-silica; the stress is controlled by the voltage applied to the piezoelectric crystal glued to the fused-silica crystal. The driving of the PEM can be assumed to be sinusoidal in nature, and is modeled by cos, the factor A then is the maximum reached at the peaks of the sinusoid, the factor is controlled by the generator AC voltage applied to the PEM. Note that it is possible to drive the PEM such that light passing through the PEM transforms past circular and back to elliptical.

$$\sin(A\cos x) \qquad \text{(3-14)}$$
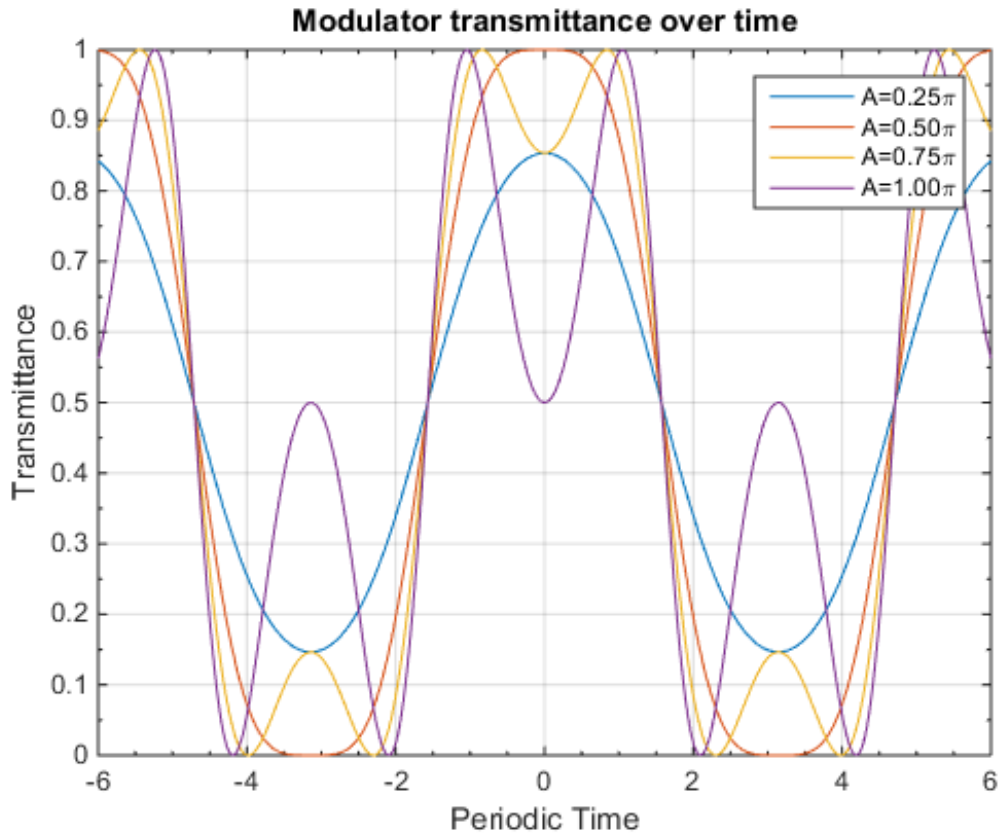
Figure 3-3: Calculated form of signal from photo-detector at different drive levels.

Distortions seen on Figure 3-3 for A greater than ½ π are due to the fact that the photoelastic modulator, when overdriven, retards the phase past what is needed for a quarter wave plate. The resultant wave would now be a non-circular ellipse. The next element, a quarter wave plate, which should have shifted the circularly polarized light back into linearly polarized light, instead shifts the elliptical polarization into elliptically polarized light. The component of light that can pass through the analyzer is then a fraction of the total and thus the amount of light passing though the setup is reduced. The opposite is true when the modulator circularity is of the opposite sign. The linearly polarized light which should be blocked by the analyzer would be presented as elliptical and thus a component of that light which is aligned to the analyzer passes through. Thus, the further away A is away from $\pm\frac{\pi}{2}$ the more distorted the observed signal is.

The amplitude of the drive on the PEM can optimized for different measurement schemes in a working cIPF. If the signal from the photo-detector is sampled at peak

modulation with a narrow sampling time, there will be a wide range of acceptable amplitudes. If the sampling occurs over a complete positive period, the amplitude can be optimized such that the average modulation in the period is maximized. This corresponds to finding the largest area under the curve over a quarter-period (0 to pi/2) i.e. (3-15). Using Equation (3-15), the optimum value for A is found numerically and the modulated light output for this value is plotted in Figure 3-5.

$$\Gamma_{optimal} = \max\left(\int_0^{\frac{\pi}{2}} \sin(A\cos x)\,dx\right) = 0.63\pi \qquad \text{(3-15)}$$
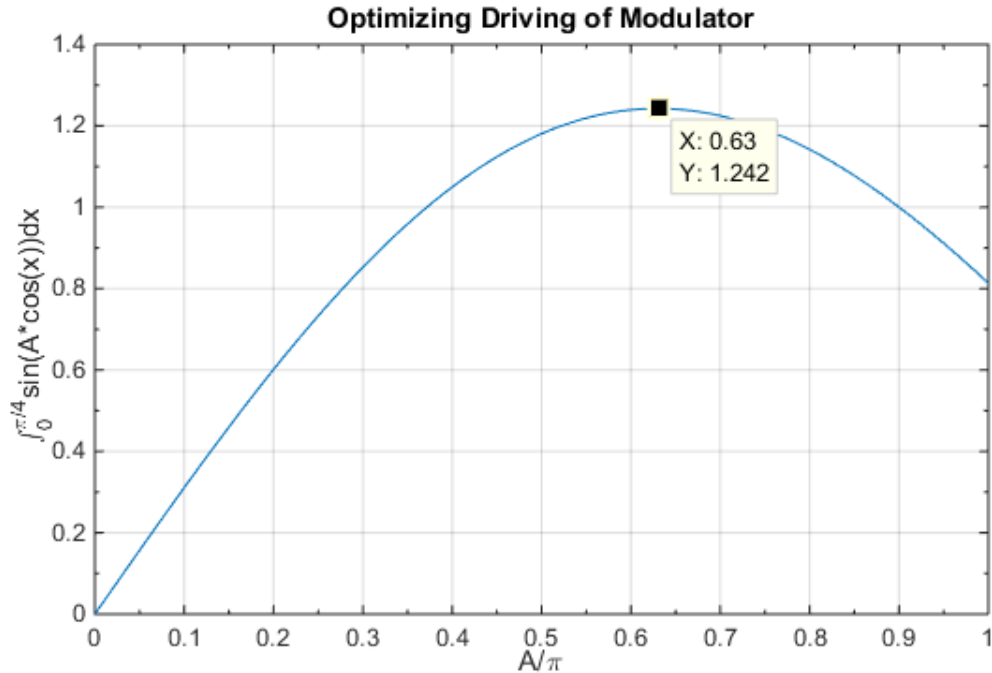
Figure 3-4: Integrating the signal shows a maximum, the optimum drive amplitude is located here.
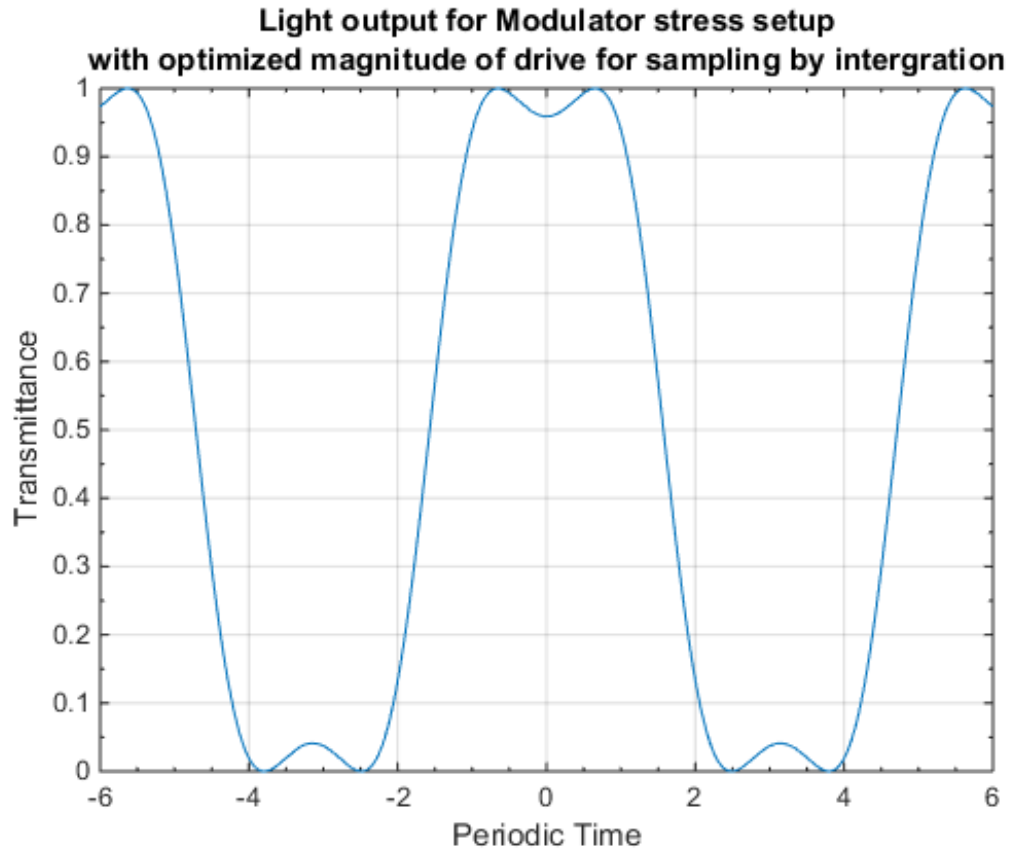
Figure 3-5: Optimized amount of stress based birefringence as seen by a polarizer, quarter wave plate, modulator, polarizer setup.

3.2 Etalon

The etalon is a block of Tellurium Dioxide which exhibits birefringence. It is used in CIPS to create an optical comb filter with fingers at regular intervals of wavelength. An overview of the etalon is presented here in section 3.2 to understand the cIPF optical structure. The study starts with an analysis of the TeO_2 refractive index. The Sellmeier equation (3-19) is used to estimate the refractive index in the wavelengths of interest. The Birefringent Filter composed of linear polarizers, etalon and PEM is then presented with different amounts of stress on the fused silica of the PEM, analogous to the operation of the cIPF in CIPS.

The correlated interference polarization spectrometer (CIPS) detects the presence of gas by using a comb filter that shifts in spectrum in time. A controlled

interference polarization filter (cIPF) is used for this function, and is developed here in this section.

The refractive index of α-TeO$_2$ (Tellurium Dioxide or paratellurite) is well measured in the wavelength range of 0.4µm to 1µm. The Sellmeier equation allows for calculations of the refractive index's dependence on the wavelength of light. It is common practice to use this equation instead of the empirical recorded data as the refractive index can be described fairly accurately with a few coefficients and describes fairly accurately the refractive index at longer wavelengths, however caution should be applied in applying this as the wavelengths of light used in CIPS could be considered far away from the valid range, the valid range being the wavelength range of 0.4µm to 1µm. [36]

Measurements of TeO$_2$ dimensions:

X	Y	Z
13.98 mm	14 mm	7.42 mm

$$\Delta N = N_e - N_o \tag{3-16}$$

N_e- index of refraction in the direction of the optic axis

N_0- index of refraction in the perpendicular to the optic axis

ΔN-birefringence

$$n_1 = d_1 \Delta N \tag{3-17}$$

n_1- relative retardation

d_1- Thickness of crystal

$$\Gamma = \frac{2\pi \Delta N L}{\lambda_0} \tag{3-18}$$

Γ-relative phase

L-thickness of crystal

λ_0-vacuum wavelength of light

Previous to sensorCAT's involvement in this project, TeO_2 refractive index in the wavelengths around 3.25µm which we are interested in has not been measured. An approximation must be found via a measured relationship between refractive index and its wavelength. The best estimate of its refractive index in this range comes from the Sellmeier equation and coefficients. [37]

The dispersion formula for TeO_2 found in literature[38] is given as:

$$n^2(\lambda) = A + \frac{B_1\lambda^2}{\lambda^2 - C_1} + \frac{B_2\lambda^2}{\lambda^2 - C_2}$$ (3-19)

$$n_0^2(\lambda) = 1 + \frac{2.584\lambda^2}{\lambda^2 - 0.1342^2} + \frac{1.157\lambda^2}{\lambda^2 - 0.2638^2}$$

$$n_e^2(\lambda) = 1 + \frac{2.823\lambda^2}{\lambda^2 - 0.1342^2} + \frac{1.542\lambda^2}{\lambda^2 - 0.2631^2}$$

Normal and extraordinary refractive indexes are plotted below in two different ranges from 0.4µm to 3.35µm and from 3.15µm to 3.35µm. Something to note here is that the refractive indexes are stable and does not vary much in the region of interest with a 0.02% difference across the range for both. The estimation of refractive indexes should hold valid for wavelengths which are far away from any regions of absorption. As seen in Figure 3-8, the transmittance curve for paratellurite is flat in the region of interest which means that there is no region of absorption in the wavelengths of interest and the Sellmeier equation should hold for this region.
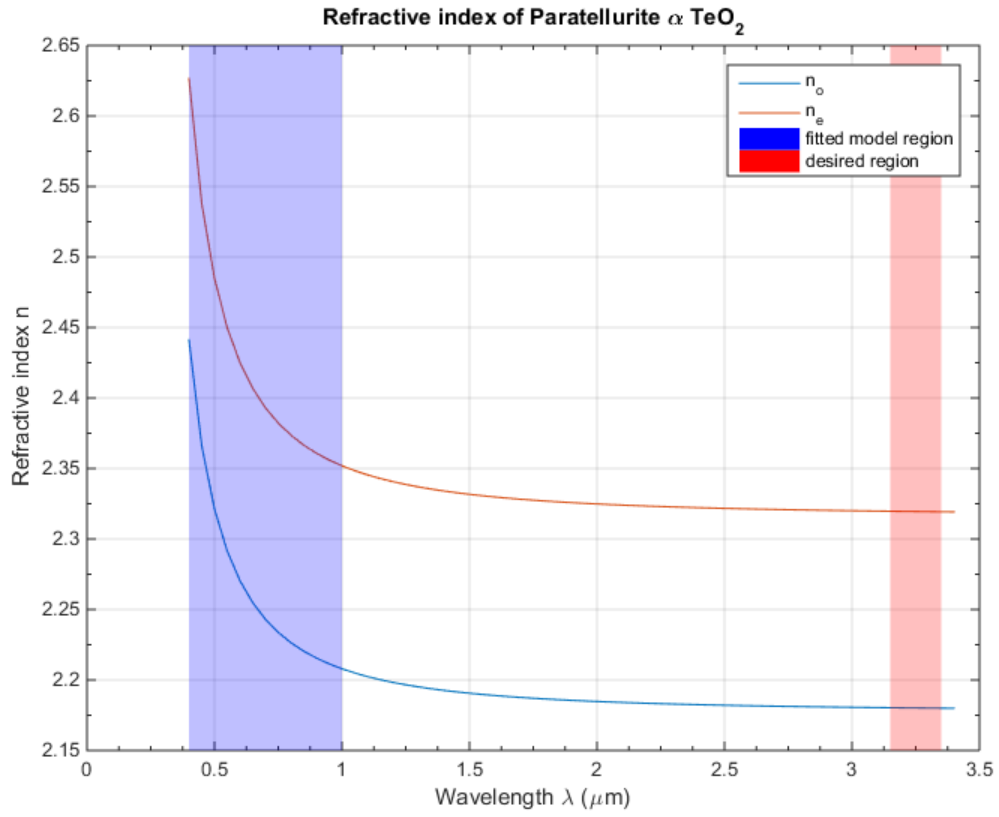
Figure 3-6: Refractive index from formula.
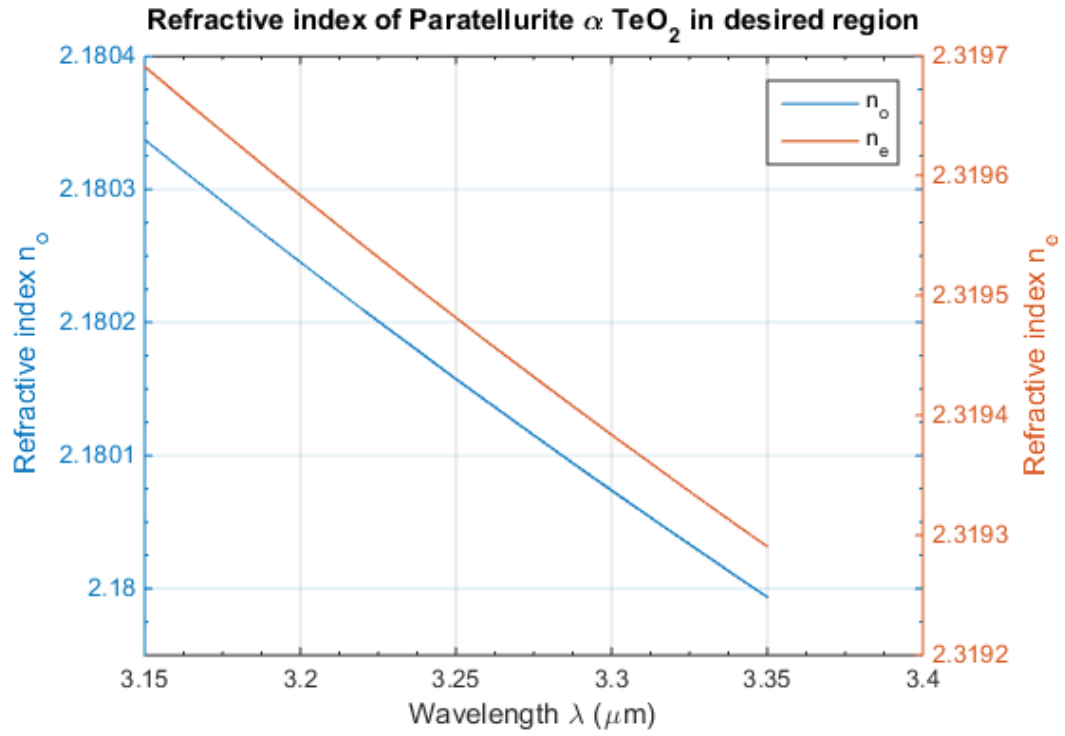
Figure 3-7: Estimated refractive index in region of interest. At 3.25μm, No is 2.180 and Ne is 2.319, thus ΔN is 0.139

TeO2 transmission, 20 mm thick sample
1 - O-polarization, 2 - E-polarization
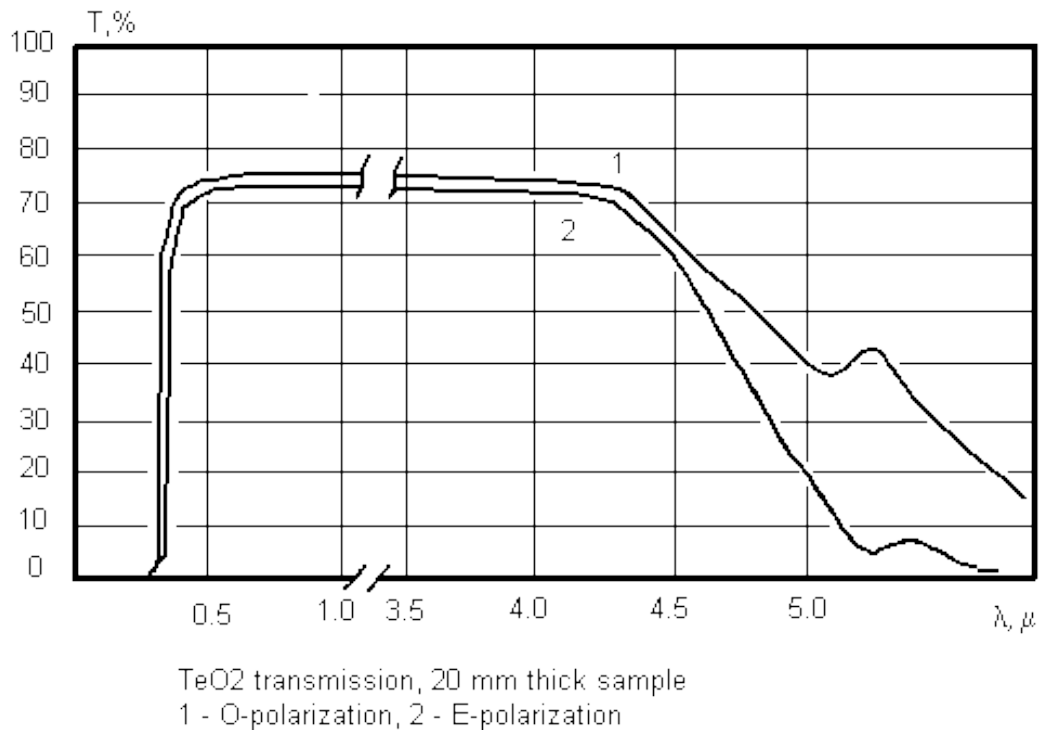
Figure 3-8: transmission curve for paratellurite(Figure taken from [39])

3.3 CIPS cIPF mathematical description

Each component of the cIPF can be described individually via either a Jones matrix (2X2) or polarized light as a Jones vector (2X1). Just like the Stokes parameters and Muller matrix, Jones calculus is a method to mathematically describe the polarization state of light and determine the effect an optical element will have on light. The tradeoff for using Jones matrix is that it can only describe polarized light and cannot describe un-polarized, partially polarized or incoherent light. In return the matrix complexity is reduced from 4x4 as in the case of the Muller matrix. The first element in the light path of cIPF is a polarizer and thus Jones matrix can be used by substituting the light source and filter with already polarized light. The Jones calculus allows us to then combine the matrixes that describe the elements in order to calculate the light output to the detector.

As a reminder the fused silica piezoelectric quartz modulator (FS quartz modulator) is described as follows:

$$\begin{bmatrix} e^{i\phi_x}\cos^2\theta + e^{i\phi_y}\sin^2\theta & \left(e^{i\phi_x} - e^{i\phi_y}\right)\cos\theta\sin\theta \\ \left(e^{i\phi_x} - e^{i\phi_y}\right)\cos\theta\sin\theta & e^{i\phi_x}\sin^2\theta + e^{i\phi_y}\cos^2\theta \end{bmatrix} \tag{3-20}$$

ϕ_x-Phase of the electric field in the X direction.

θ-Orientation of fast axis for modulator

A linear polarizer oriented -45° is described as:

$$\frac{1}{2}\begin{bmatrix} 1 & -1 \\ -1 & 1 \end{bmatrix} \tag{3-21}$$

And linearly polarized light oriented at 45° is:

$$\frac{1}{\sqrt{2}}\begin{bmatrix} 1 \\ 1 \end{bmatrix} \tag{3-22}$$

For CIPS the crystal is oriented at 90° and the phase in the y direction is zero and the modulator reduces to:

$$\begin{bmatrix} 1 & 0 \\ 0 & e^{i\phi_x} \end{bmatrix} \tag{3-23}$$

ϕ_x-Phase of the electric field in the X direction.

The phase of the electric field varies linearly with stress in the FS, and the stress in the FS quartz modulator is sinusoidal:

$$\phi_x = A * \sin(\omega t) \tag{3-24}$$

A-Amplitude of stress

ωt-angular displacement of stress

The cIPF uses an etalon to generate the fine comb-like structures in the filter. The etalon uses the same type of birefringent spectral filter (BSF) as the ones in lyot filters and can be considered and analyzed as a single stage lyot filter.

The etalon acts as a retarder where the phase shift is described as follows:

$$\phi = \frac{2\pi e \Delta n}{\lambda} \tag{3-25}$$

ϕ-phase shift

e-thickness

Δn-birefringence

λ-wavelength

And the etalon is described as:

$$\begin{bmatrix} \cos\frac{1}{2}\phi + i\cos 2\theta * \sin\frac{1}{2}\phi & i\sin\frac{1}{2}\phi\sin 2\theta \\ i\sin\frac{1}{2}\phi\sin 2\theta & \cos\frac{1}{2}\phi - i\cos 2\theta * \sin\frac{1}{2}\phi \end{bmatrix} \tag{3-26}$$

θ- Orientation of fast axis for etalon

Since the cIPF has a linear polarizer as the first element, Jones matrix can be used; the first polarizer can be omitted and the incident light source can be described as a linearly polarized light source. Light that passes through the cIPF should have a Jones vector as an output. The transmission intensity of light will be proportional to the sum of the squares of the magnitude of the two components of the resultant Jones vector. [40]

The CIPS controlled interference polarization filter (cIPF) is then described as:

-45°   Etalon   Modulator   Polarized   (3-27)

Linear   light 45°

analyzer

$$\frac{1}{2}\begin{bmatrix} 1 & -1 \\ -1 & 1 \end{bmatrix} \cdot \begin{bmatrix} \cos\frac{1}{2}\phi + i\cos 2\theta * \sin\frac{1}{2}\phi & i\sin\frac{1}{2}\phi\sin 2\theta \\ i\sin\frac{1}{2}\phi\sin 2\theta & \cos\frac{1}{2}\phi - i\cos 2\theta * \sin\frac{1}{2}\phi \end{bmatrix} \cdot \begin{bmatrix} 1 & 0 \\ 0 & e^{i\phi_x} \end{bmatrix} \cdot \frac{1}{\sqrt{2}}\begin{bmatrix} 1 \\ 1 \end{bmatrix}$$

The fast angle θ is oriented at 0° for the etalon and so the etalon matrix is simplified:

$$\frac{1}{2}\begin{bmatrix} 1 & -1 \\ -1 & 1 \end{bmatrix} \cdot \begin{bmatrix} \cos\frac{1}{2}\phi + i*\sin\frac{1}{2}\phi & 0 \\ 0 & \cos\frac{1}{2}\phi - i*\sin\frac{1}{2}\phi \end{bmatrix} \cdot \begin{bmatrix} 1 & 0 \\ 0 & e^{i\phi_x} \end{bmatrix} \cdot \frac{1}{\sqrt{2}}\begin{bmatrix} 1 \\ 1 \end{bmatrix} \qquad \text{(3-28)}$$

The resultant Vector is then:

$$\frac{1}{2\sqrt{2}}\left(1 + e^{i\phi_x}\right)\left(\cos\frac{\phi}{2} + \sin\frac{\phi}{2}\right)\begin{bmatrix} 1 \\ -1 \end{bmatrix} \qquad \text{(3-29)}$$

3.4 Simulated Transmission spectrum of cIPF

The transmission spectrum is simulated on MATLAB for when the PEM acts as a quarter wave plate and generates right hand (RH) and left hand (LH) circularly polarized light in the wavelengths of interest from 3.15µm to 3.35µm using equation (3-25) and a closer plot (Figure 3-9) is provided such that the sinusoidal pattern is more visible from 3.22µm to 3.29µm. These plots are provided to show the output spectrum of the cIPF at two static moments in time.
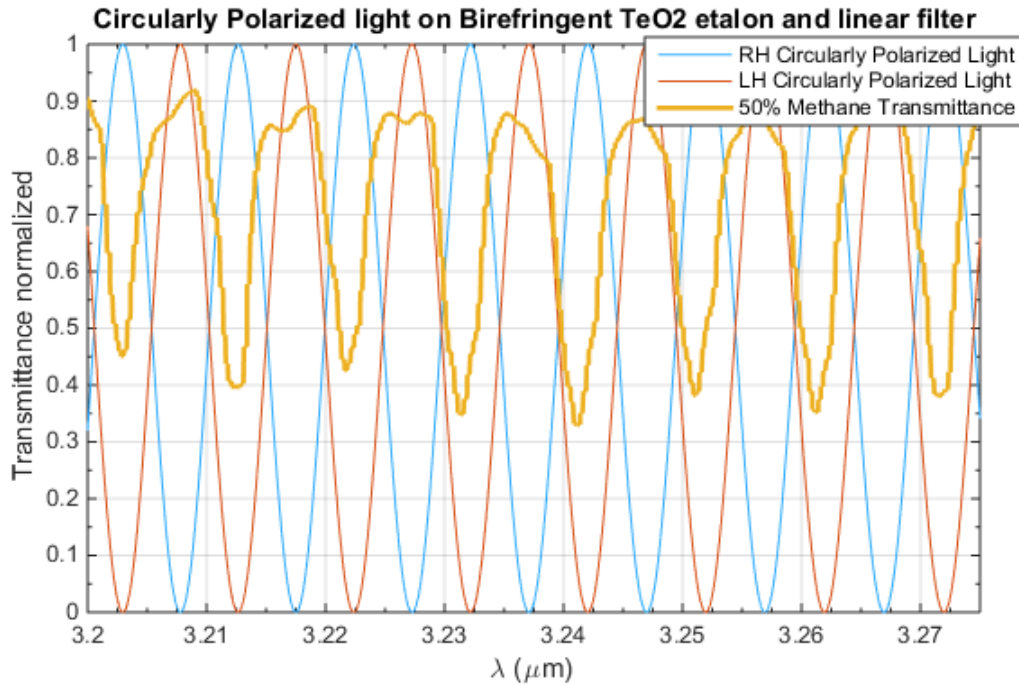
Figure 3-9: Transmission spectrum for cIPF when modulator retards light to circular polarization for wavelengths between 3.2µm to 3.275µm (50% Methane Transmittance spectrum provided by Dr. Olga Kosobokova)

The CIPS cIPF is also plotted where the stress on the PEM varies sinusoidally much like in the CIPS device itself in operation. Amplitudes of stress are varied below, each corresponding to different amounts of stress induced birefringence magnitudes with identical frequencies of modulation, as in the case with the actual CIPS device. The thickness of the etalon was also altered such that peaks from circularly polarized light are aligned to the peaks of methane. The response is calculated for the cases with and without the spectrum of transmittance of 50% methane. The methane transmittance data was collected from experiments done by Dr. Kosobokova. The total amount of light on the photo-detector was calculated by summing up the transmittance of the cIPF at each point in periodic time. An ideal pass-band filter was added which limits the detection region from 3.1936 µm to 3.2823 µm which corresponds to nine intervals or bands from the etalon.
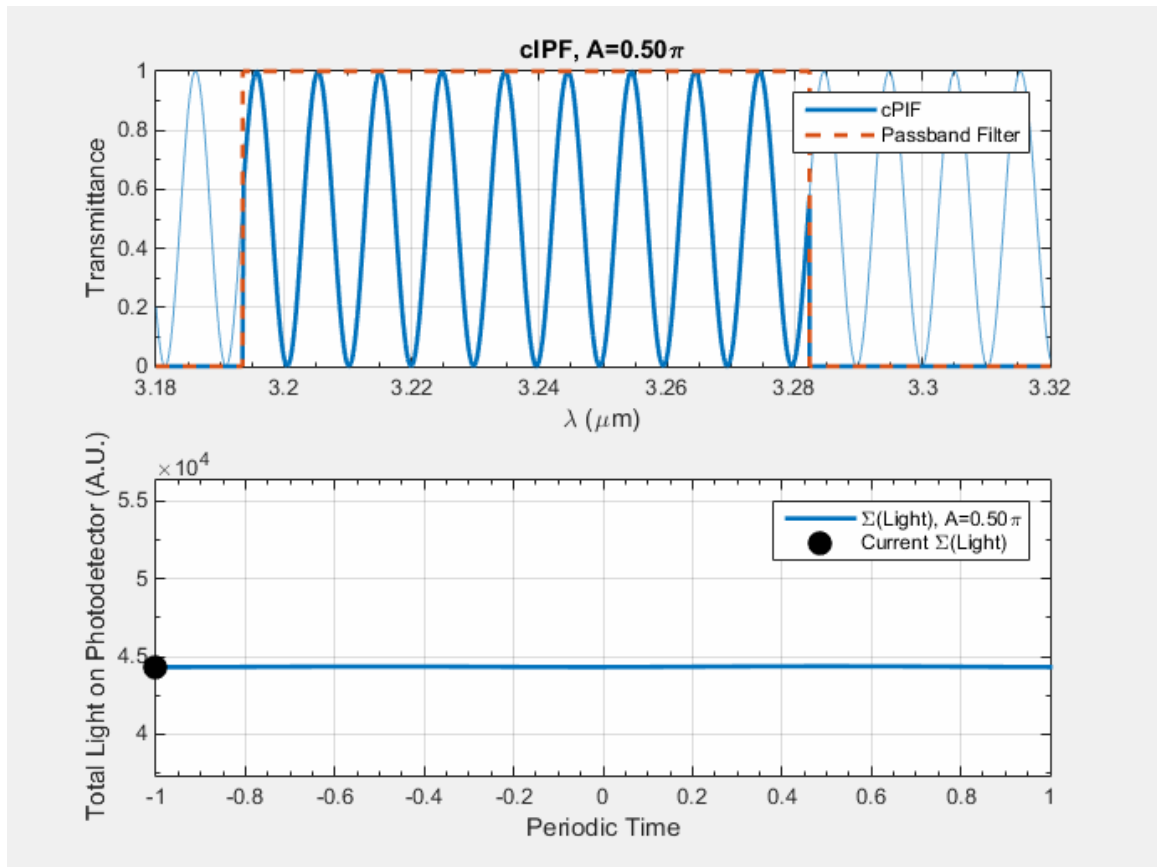
Figure 3-10: CIPS cIPF output with modulator at 100%.

Figure 3-10 is provided as a reference to show the signals observed without the presents of methane. As the comb filter moves, the average light output stays stable. Since only the difference of the signal in time is measured when CIPS is operating, the stable output corresponds to zero measured methane.
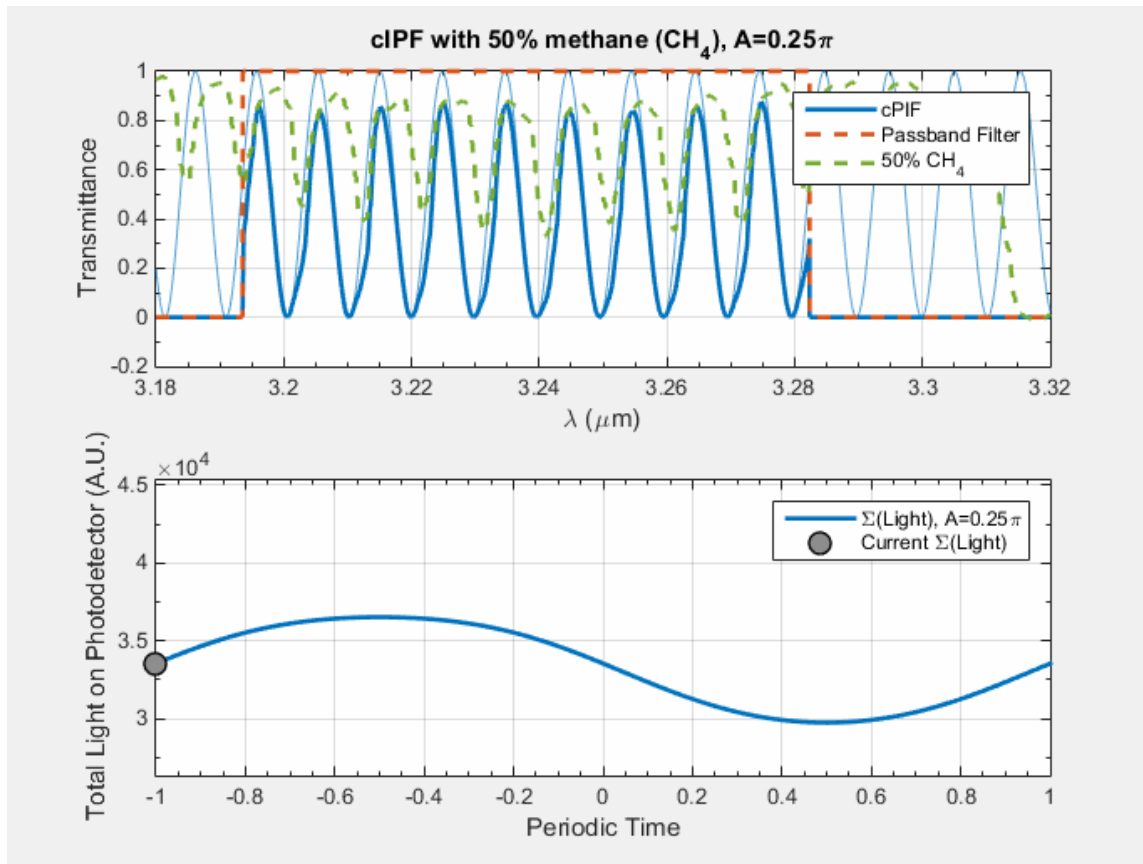
Figure 3-11: CIPS cIPF output with 50% methane and modulator at 50%.

With methane introduced into the optical path, the cIPF output, seen as the total light on photo-detector, changes over time. This change detected is what is used to compute the concentration of methane gas. A photoelastic modulator at what is deemed 50% is only able to create elliptically polarized light but it is enough to show the operation of the cIPF (see Figure 3-11). The peaks of the comb filter moves on the slopes of the methane spectrum and it is the combination of the two spectrums, one which is moving and the other stationary that produces the waveform seen at the bottom of the chart.
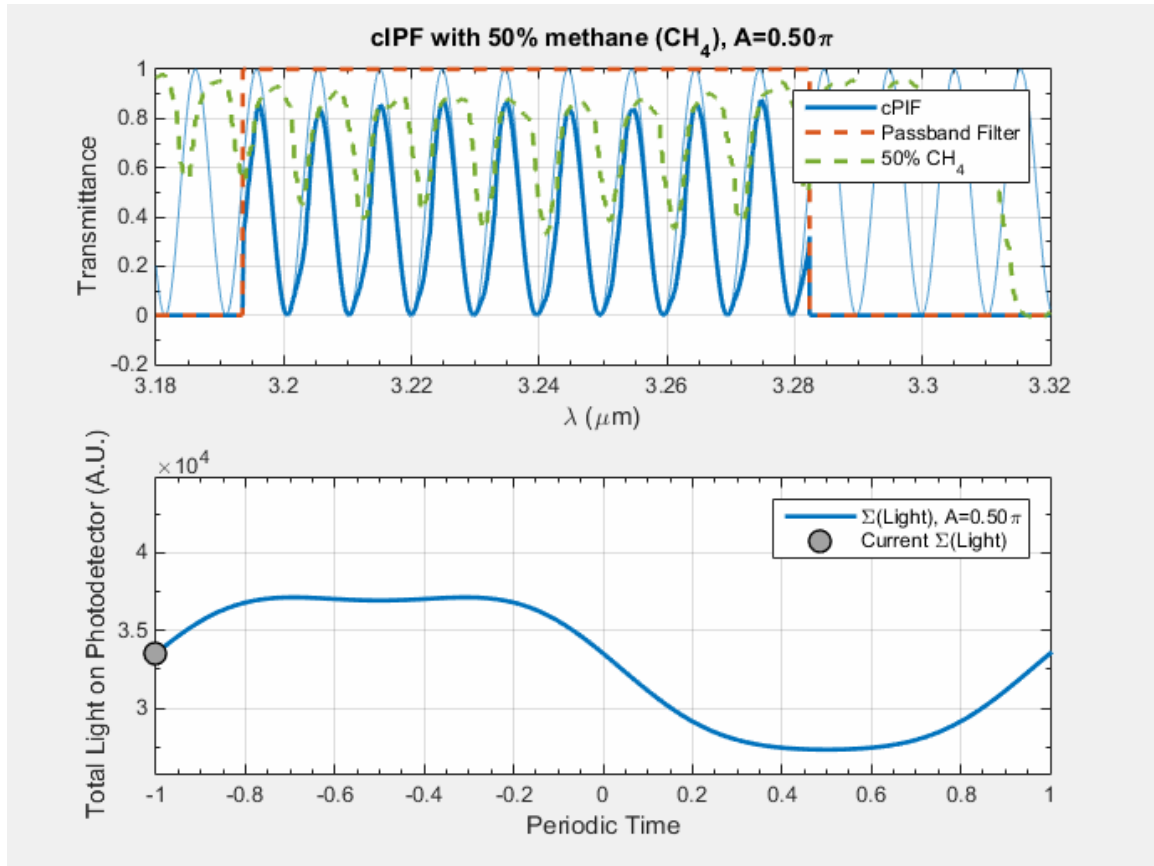
Figure 3-12: CIPS cIPF output with 50% methane and modulator at 100%.

The modulation has been increased to 100% in Figure 3-12 which corresponds to the modulator forming circularly polarized light from the linearly polarized light. This is what should be the proper operational range of the modulator in the cIPF if not close to the optimum amount of modulation, Equation (3-15). The asymmetry of the total light on photo-detector is due to the non-sinusoidal spectrum of methane.
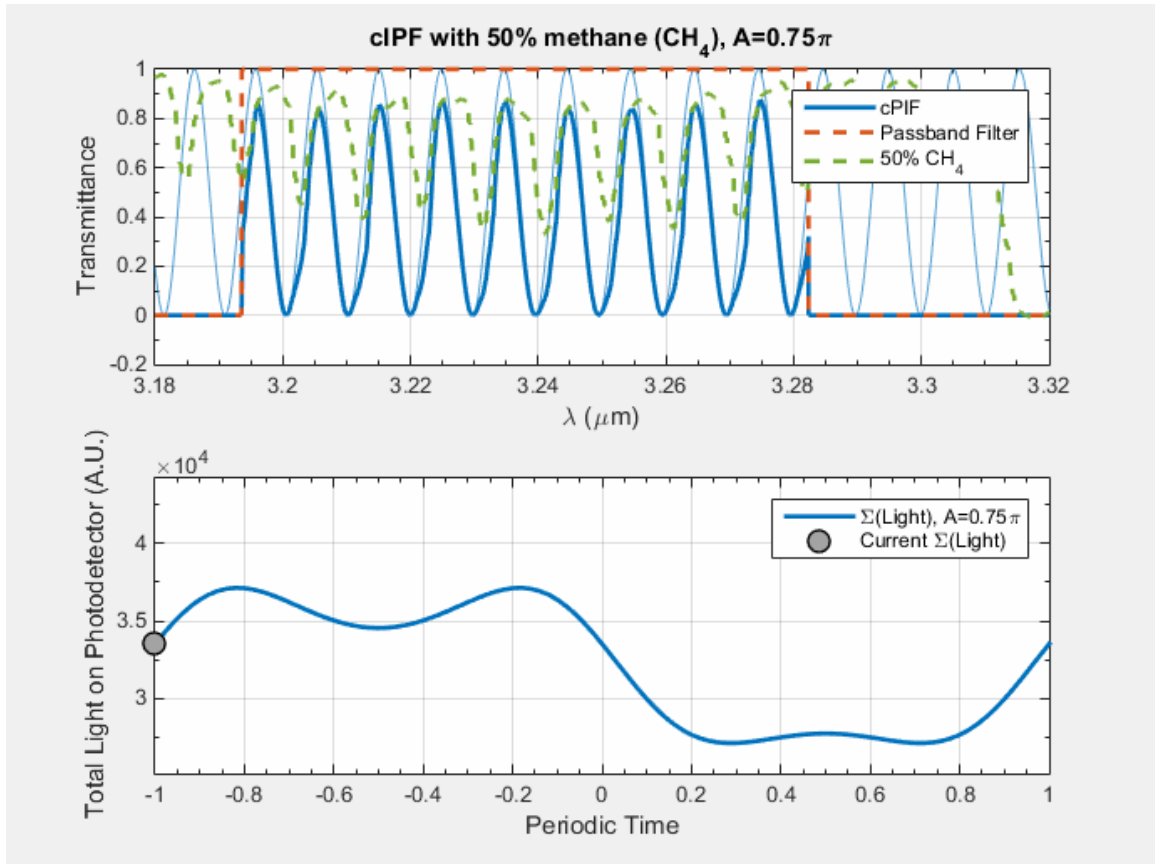
Figure 3-13: CIPS cIPF output with 50% methane and modulator at 150%.
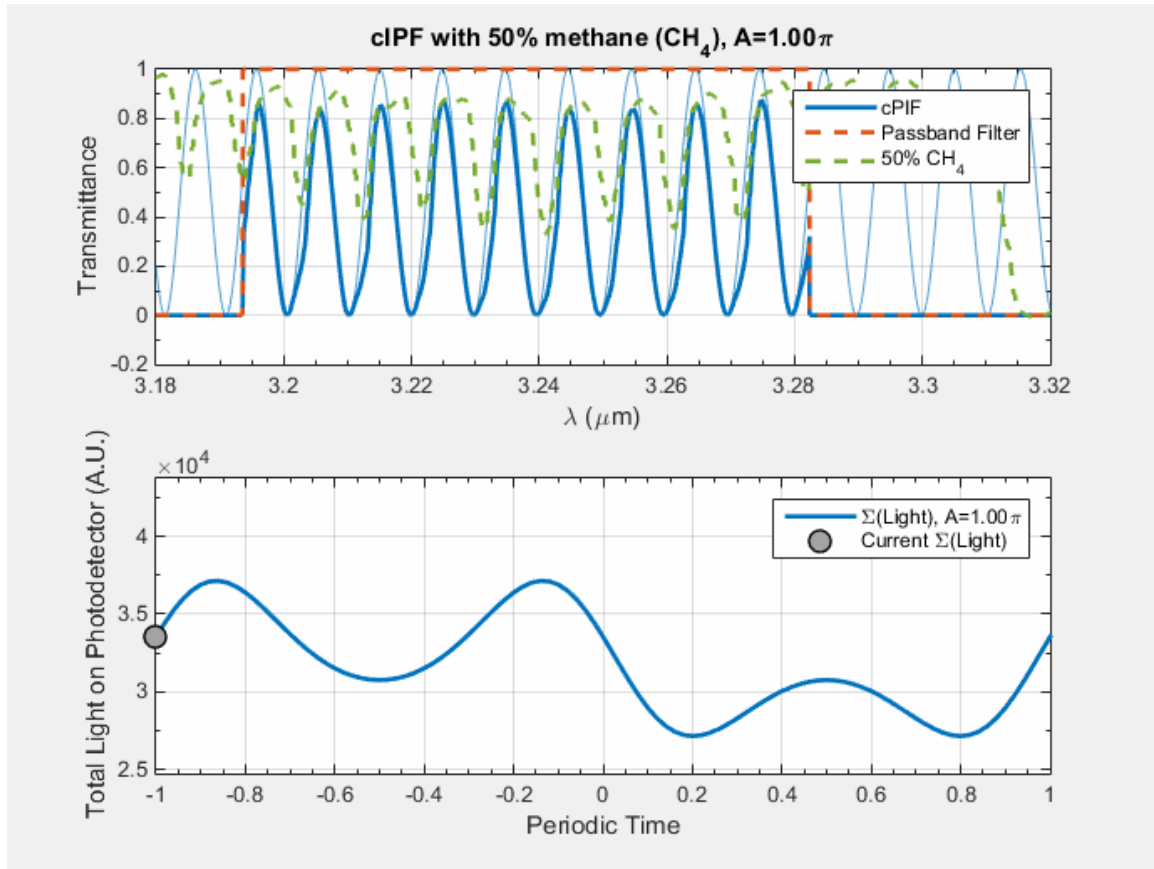
Figure 3-14: CIPS cIPF output with 50% methane and modulator at 200%.

The simulation results give us more insight on the operation of the cIPF and observed light output on the photo-detector. The total light incident over time on the photo-detector will be the waveform seen from the photo-detector and is calculated from the sum of the total transmittance across all wavelengths. The effect of over-modulating, as in the case where power to the PEM is increased past the optimum point (shown in Figure 3-13 and Figure 3-14) will result in shifting the comb filter such that the features line back with the comb filter at another point in time. As the amplifier stage of the CIPS samples the signal at those points in time, the effect is that over-modulation decreases the correlation and thus decreases sensitivity. Figure 3-14 shows that the cIPF could be completely insensitive to the presence of methane if sampling takes place only at -0.5 and 0.5 in periodic time.

Chapter 4   Optimization of CIPS based opto-electronic methane detector

Birefringence is the difference in refractive index between polarized light whose polarization is perpendicular to the direction of the optical axis and polarized light whose polarization is in the direction of the optical axis. Fused silica exhibits birefringence when stressed (i.e. stress induced birefringence), the stress birefringence relationship is linear below its plastic deformation region.[41] In the cIPF, the stress on the FS is created by the quartz, the stress is induced sinusoidally and the stress magnitude determines the maximum amount of birefringence in the FS. To determine the amount of stress, a measurement was performed to measure the stress-optic coefficient.[42]

$$\Delta = \frac{2\pi t}{\lambda} C(\sigma_1 - \sigma_2) \tag{4-1}$$

σ_1, σ_2-first and second principal stresses

C-stress-optic coefficient

t-thickness

λ-wavelength

Δ-induced retardation

The change in polarization measured can then be used to estimate the stress on the FS using Equation (4-1).
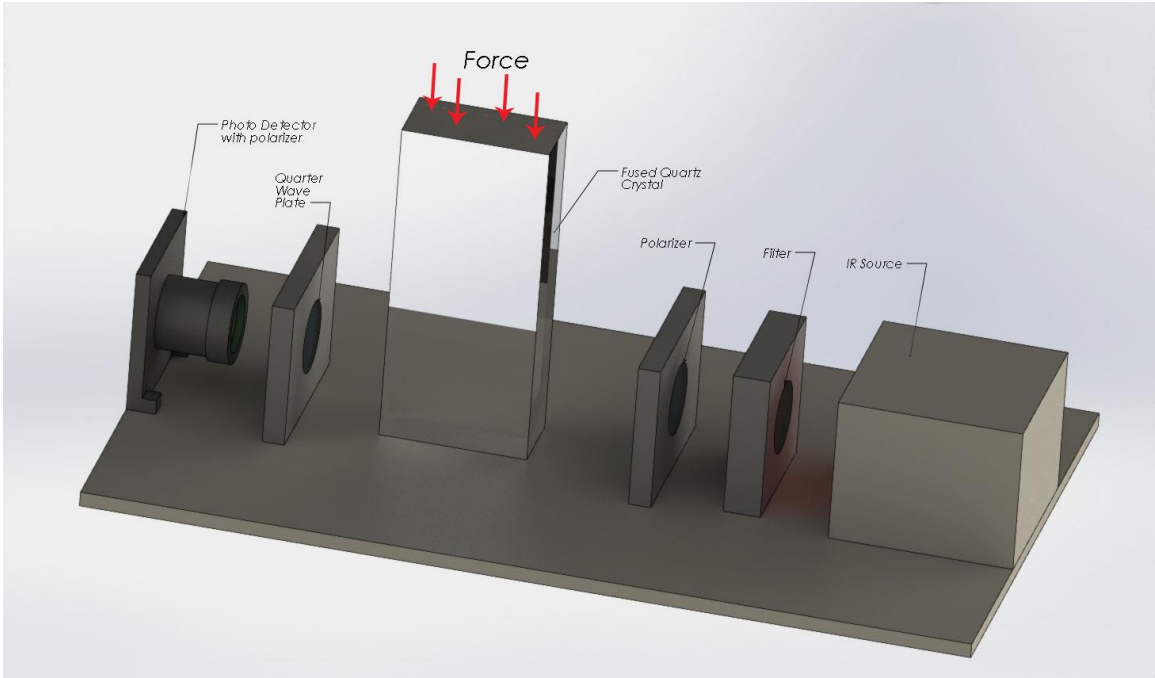
Figure 4-1: Experimental Setup. Force is applied by adding weight on top of the Fused Silica.
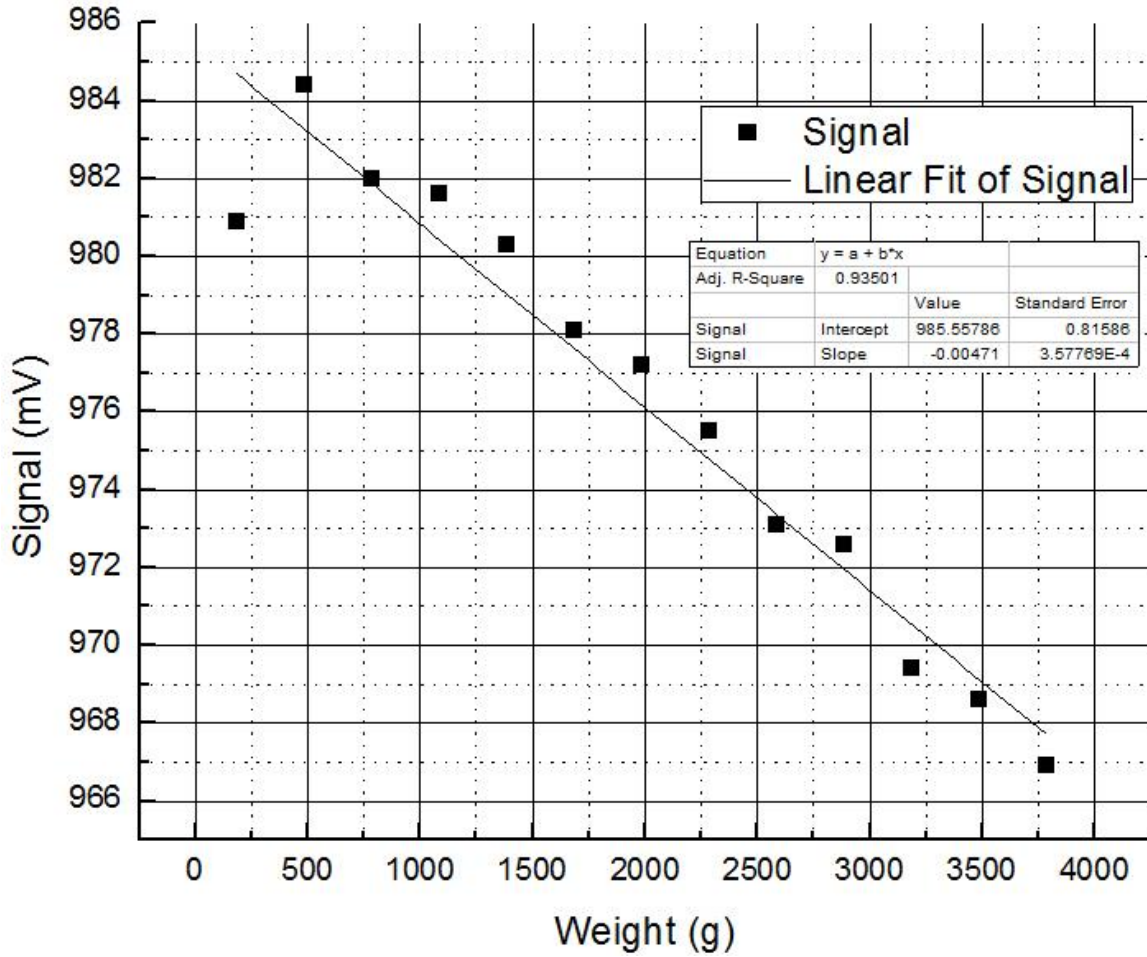
Figure 4-2: UMPD signal as it is loaded with weight.

In this measurement, the FS is compressed with force applied using weights. The induced birefringence is measured using a setup reconfigured from the existing cIPF components and a quarter wave plate. As birefringence is wavelength dependent, the setup reusing these components guarantees that the measured birefringence is accurate and appropriate. Light from an IR light source is band pass filtered and passed through a polarizer, this creates narrow band wavelengths of polarized light which has its state of polarization changed by both the fused silica, who's birefringence changes with the amount of weight and the quarter wave plate who's birefringence is static. A polarizer/analyzer is placed before the photo-detector at 90° from the other polarizer. The setup then can measure the amount of birefringence generated by an amount of static weight placed on the Fused Silica via the signal from the photo-detector. The

change in signal is compared to signal gathered from the cIPF with the PEM powered from the generator and a quarter wave plate introduced in the optical path. The amount of force applied by the PEM and generator setup is then calculated from the photo-detector signal and the relationship between photo-detector signal and force applied in the statically loaded setup.

Table 4-1: Calculating Force on Fused silica.

Modulator (Amplitude)	From measurements, UMPD Signal (V)	4.04
Position X(0) to X(max)	Modulator/2	2.02
Slope of signal to weight (μV/g)	From Linear Fit of figure	-4.71
Slope of signal to force (V/N)	Slope of signal to weight/(1e-3*9.81)	-4.80E-04
force Modulator applies (N)	Position X(0) to X(max)/Slope of signal to force	4.21E+03

4.1 Prediction of displacement of Modulator face normal to the X-axis

From Table 4-1, the PEM applies around 4.21 kN of force while working. Fused silica in general has a Young's Modulus of 71.7 GPa. From this, we can estimate the displacement of the face normal to the X-axis as:

$$F = \frac{EA_0\Delta L}{L_0} \tag{4-2}$$

$$\Delta L = \frac{FL_0}{EA_0} = \frac{4206N * 45\,mm}{71.7\,GPa * 10mm * 20mm} = 13.20\,\mu m \tag{4-3}$$

F-Force

E-Young's Modulus

A_0-Area of face

ΔL- Change in length

37

L_0-Initial length

The crystal's face should have a total displacement of 13.2 μm from (4-3) if the FS used in cIPF has the same Young's modulus.

4.2 Interferometry

Young's modulus for the FS is a material property necessary for calculating the resonant modes and frequencies and ultimately the birefringence generated from the PEM. This property is given approximately for the fused silica material, however it varies depending on manufacturing methods. As a reminder to the reader, the Young's modulus can be determined from measuring the displacement seen for a given amount of force. Since the expected displacement is a few micrometers, a method of measuring small distances is needed. The measurement system should minimally load the PEM, thus not affecting the parameters of operation. Another criterion on the measuring system is that it should be have sufficient bandwidth to measure the displacement which occurs at a frequency of around 66 kHz. A Michelson Interferometer is employed here to measure small displacements in the PEM without loading and influencing the measurement. A face of the fused silica was polished and titanium and gold deposited to form a mirrored surface. This is the only change to the PEM and such a small deposition of metal would have no appreciable effect on the PEMs function and presents a minimal weight load. In a Michelson interferometer, the optical path difference between the two mirrors is $2\Delta d$. If the difference is an integral number of wavelengths, the detector should receive the maximum intensity of light as the laser light constructively interferes. When the optical path difference is $\frac{\lambda}{2}$, there is destructive interference and a minimum intensity of light is seen. The intensity of light then varies sinusoidally as the distance changes. However an upper bandwidth requirement is imposed on the data collection side (photo-detector and oscilloscope) since every integer multiple of wavelength displacement multiplies the frequency by that integer number, see Figure 4-4.

$$2\Delta d = n\lambda \qquad\qquad (4\text{-}4)$$

Δd- Change in distance, n-integer, λ-wavelength
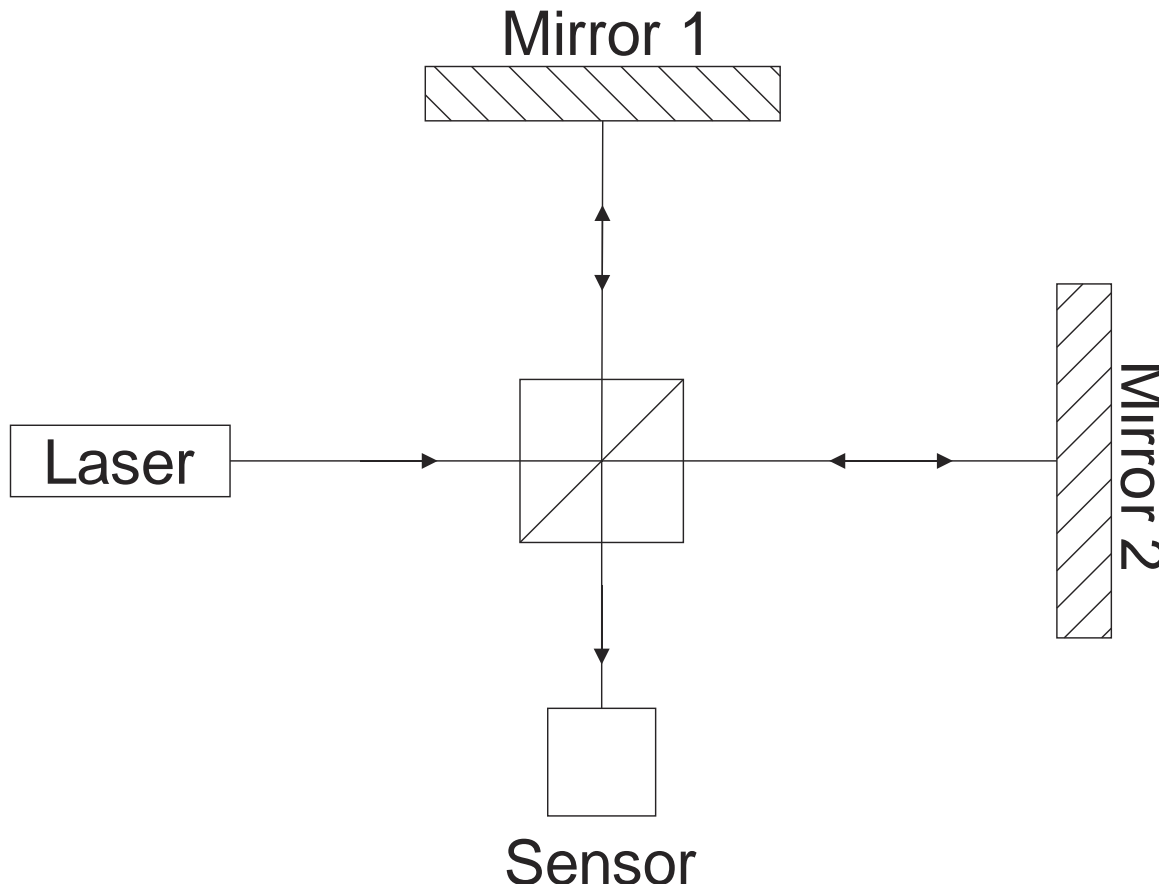
Figure 4-3: Michelson interferometer, movement in either mirror can be measured by the sensor as a change in intensity of light.
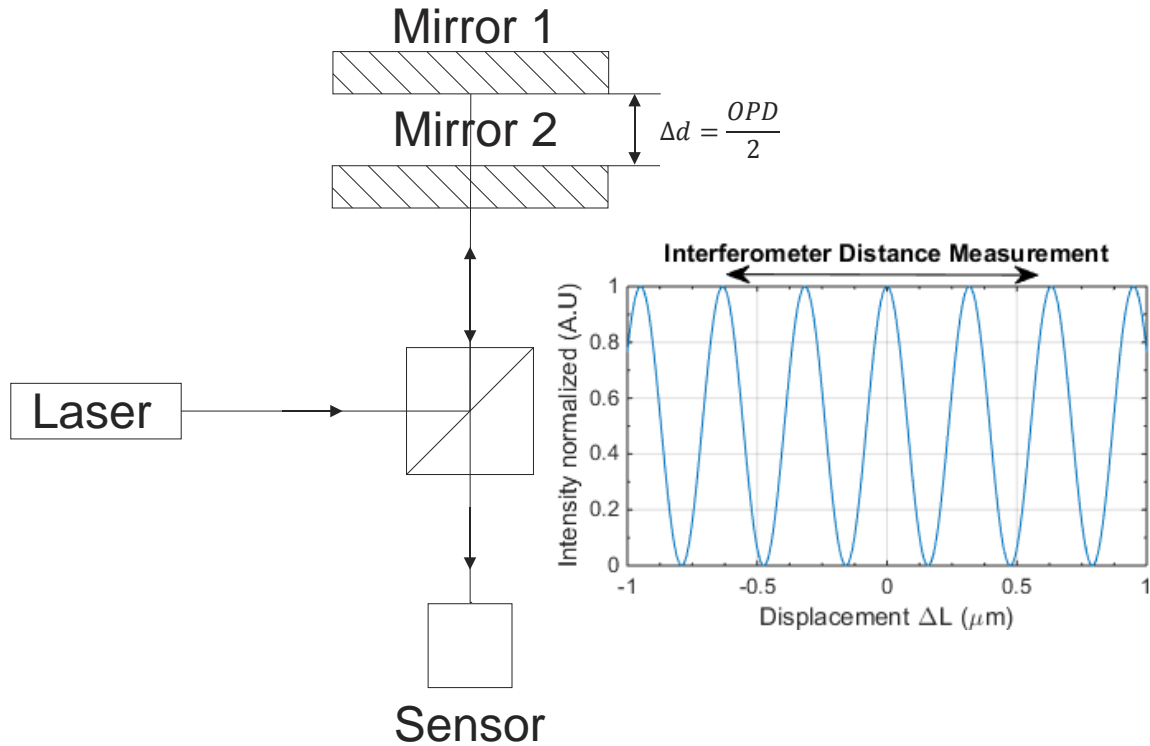
Figure 4-4: folded view of Michelson interferometer showing relationship between the relative distances of mirrors and optical path distance (OPD)

The Melles Griot HeNe laser (05-SRP-810) was used with a wavelength of 632.8 nm and with a 00 mode beam; TEM00 (>90%). This means we can measure the change in distance to the fused silica crystal at a resolution of at least half the wavelength i.e. 0.3164 microns. All of the necessary components of the setup were fabricated and the setup was first tested as shown in Figure 4-5 with a movable mirror linked to a linear micrometric linear actuator (National Aperture, Inc. MM-4MEX-110 S/N16379 and National Aperture, Inc. Servo 3000) via a class two lever. The lever has the force applied on the same side as the load and the lever divides any movement by nine. The laser beam initially was expanded with a concave lens to expedite alignment; this lens was removed for the measurement setup to increase the intensity of light. A photo-detector (New Focus Inc. Model 1621) with a nanosecond rise time and band width of more than 500MHz is used as the sensor and outputs its signal to a Tektronix MSO 4054 Mixed Signal Oscilloscope. After the verification that this setup could indeed measure distance,

the components of the setup were rearranged so that the stationary mirror is replaced with the mirrored face of the FS in the photoelastic modulator. The movable mirror, lever and actuator setup was kept and rearranged to aid in calibrating and adjusting the new setup.
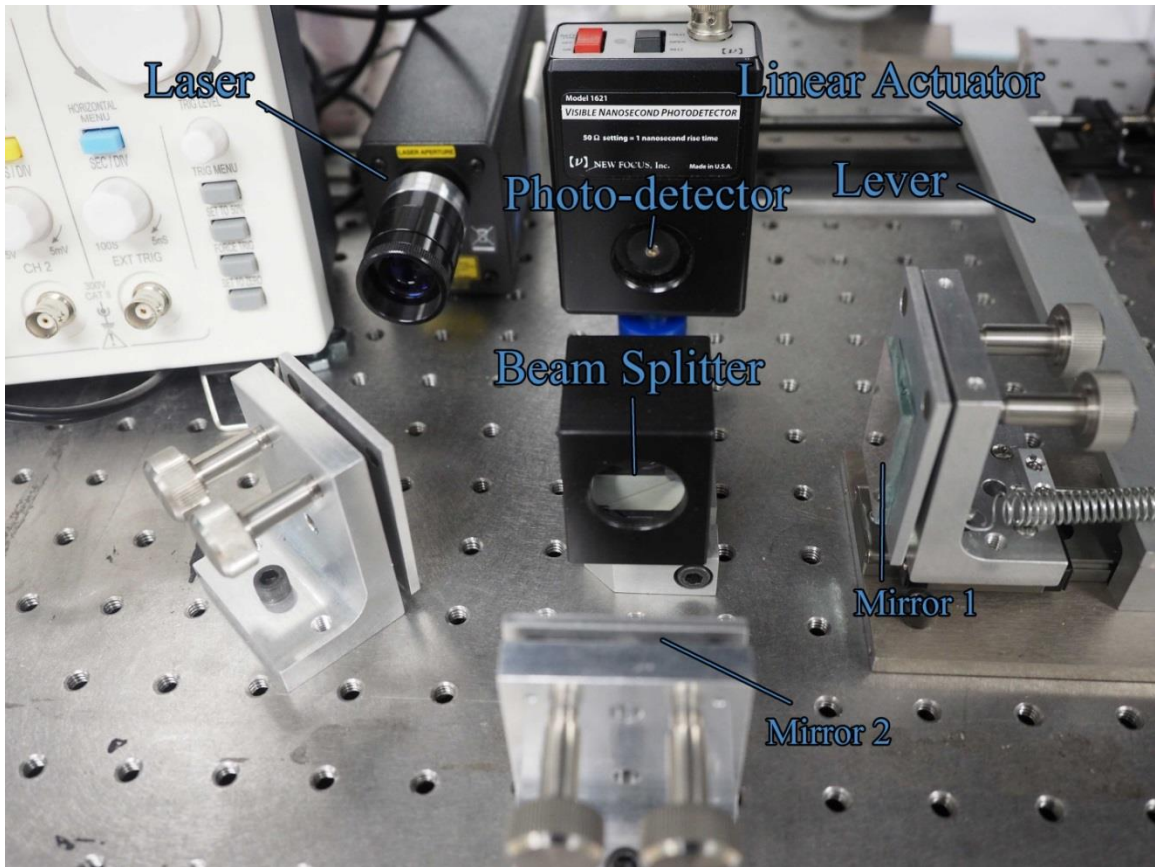
Figure 4-5: Interferometer verification setup.

The data was then collected with the Tektronix MSO 4054 sampling with 100K data points, at the maximum bandwidth of 1GHz. Measurements were taken, varying the generator supply voltage from one volt to eighteen volts in one volt increments. The amplitude of AC voltage on the modulator is directly controlled by the generator supply voltage. The supply voltage, voltage on the modulator and the signal from the photo-detector were captured on the Tektronix MSO 4054 oscilloscope and saved to a CSV file. The number of cycles determined from the photo-detector signal are then converted to displacement and finally plotted against the voltage amplitude on the modulator.
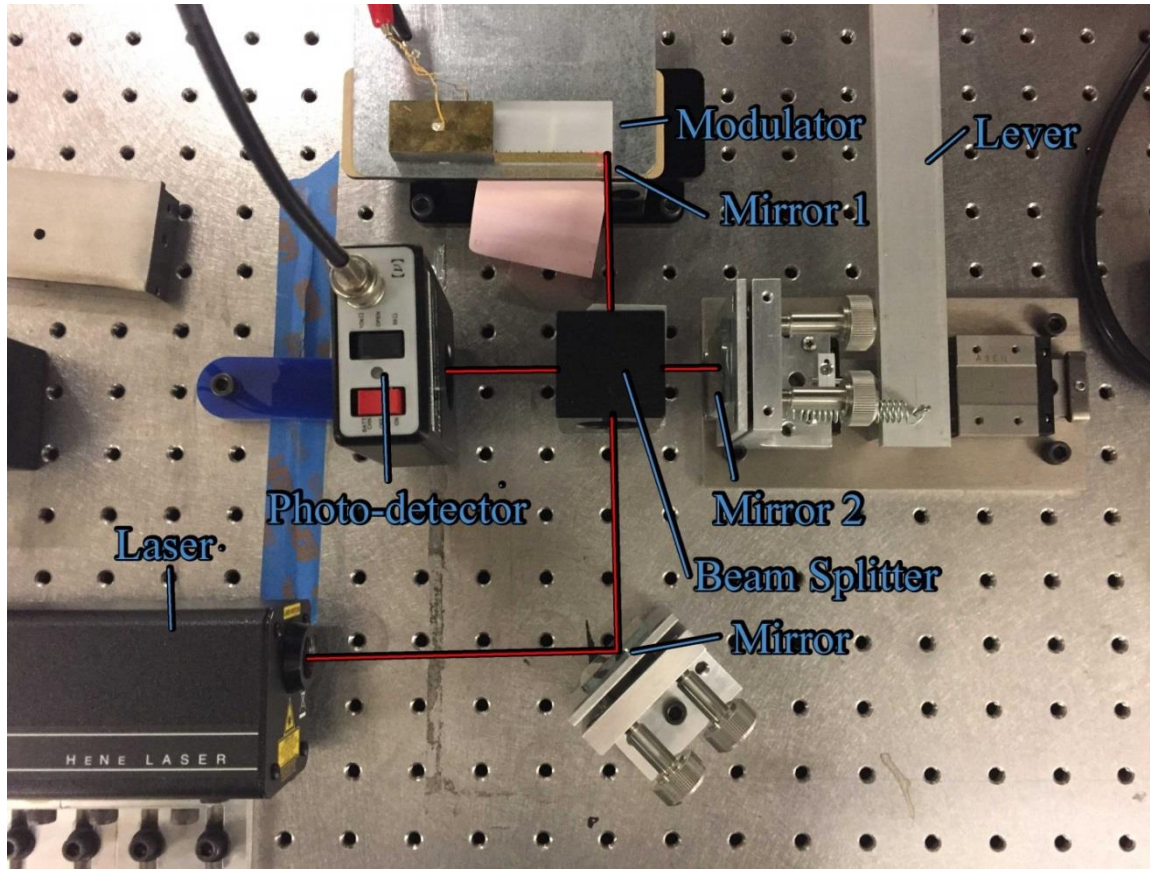
Figure 4-6: Interferometer setup to measure displacement in the face normal to the Y axis (section 4.3), the setup for displacement in the face normal to the X-axis is similar, but with the modulator rotated so that the laser beam reflects off that face.

The interferometer setup is used to measure small displacements on the PEM. Its layout is as follows: All of the components of the interferometer setup are adjusted such that the z heights are roughly aligned to be equal. The laser is mounted on its side via several angle brackets so that the z height of the laser beam is comparable to the heights of the other components. The first mirror is used to adjust and aim the laser beam from the source into the beam-splitter. Mirror 2 has the ability to move using the linear rail, lever and linear actuator. This allows the interferometer to be tested with a known displacement after the optical components are aligned, without perturbing the optical alignment. Displacement on mirror 2 and mirror 1 can then be measured by counting the cycles on the photo-detector through waveform capture on the oscilloscope.
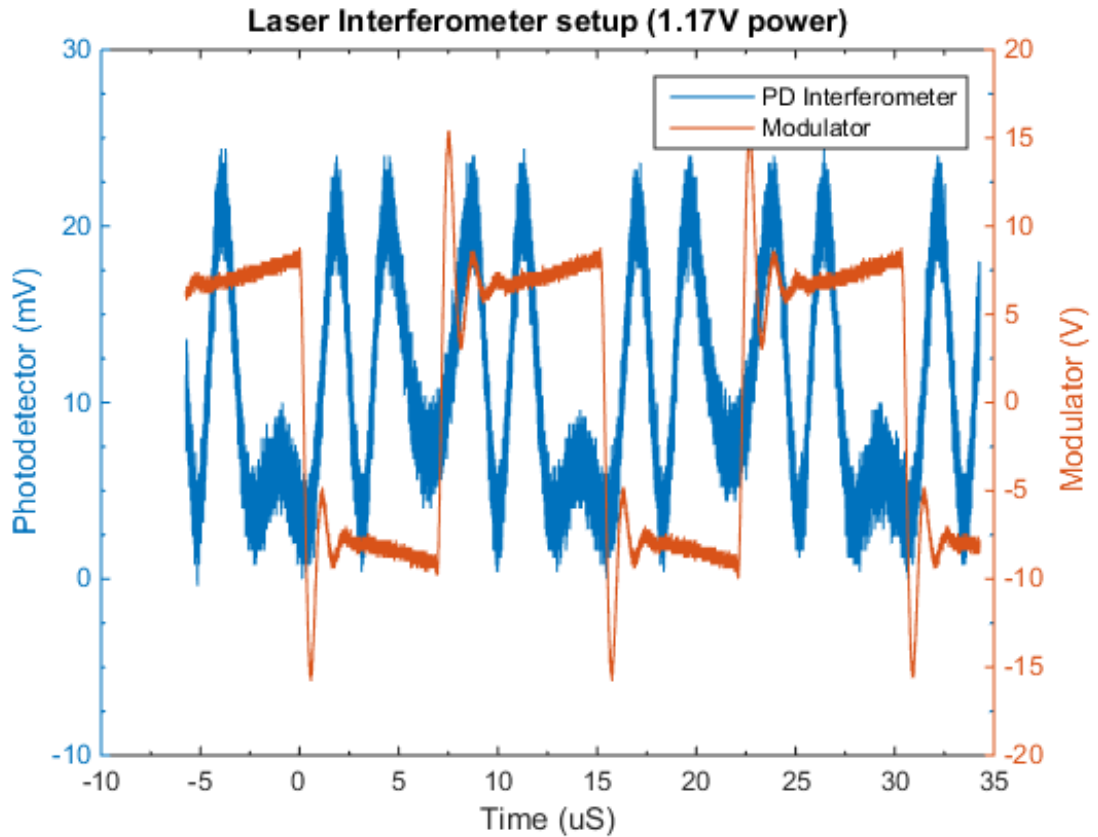
Figure 4-7: Sample capture from Tektronix MSO 4054 Mixed Signal Oscilloscope. The number of peaks in a cycle corresponding to the modulator cycle determines the displacement.

From Figure 4-7 the amount of displacement can be determined from the PD interferometer signal. A resolution of up to 1/4 the wavelength of laser light at 632.8nm, or in other words 158 nm, can be achieved when both the numbers of periods as well as the partial levels reached at peak displacement are taken into account, this is akin to being able to count with more precision by estimating the distance between the finest lines of a ruler.
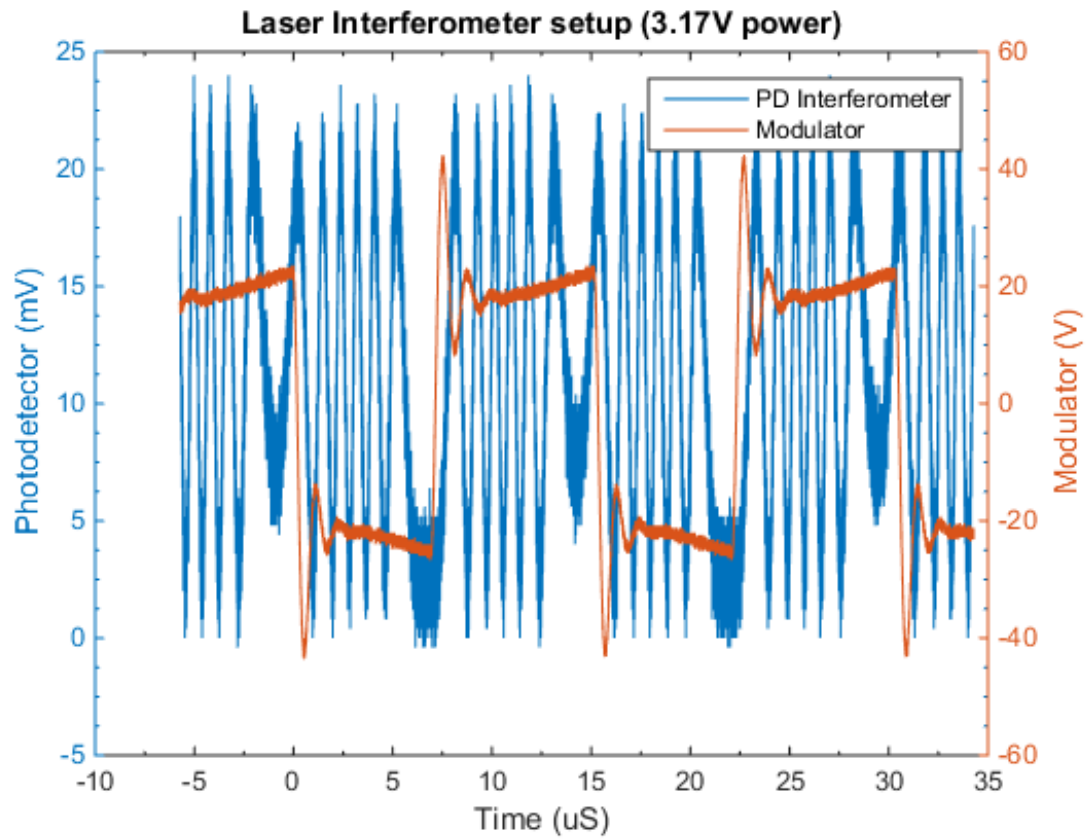
Figure 4-8: Sample capture from Tektronix MSO 4054 Mixed Signal Oscilloscope. The number of peaks in a cycle corresponding to the modulator cycle determines the displacement.
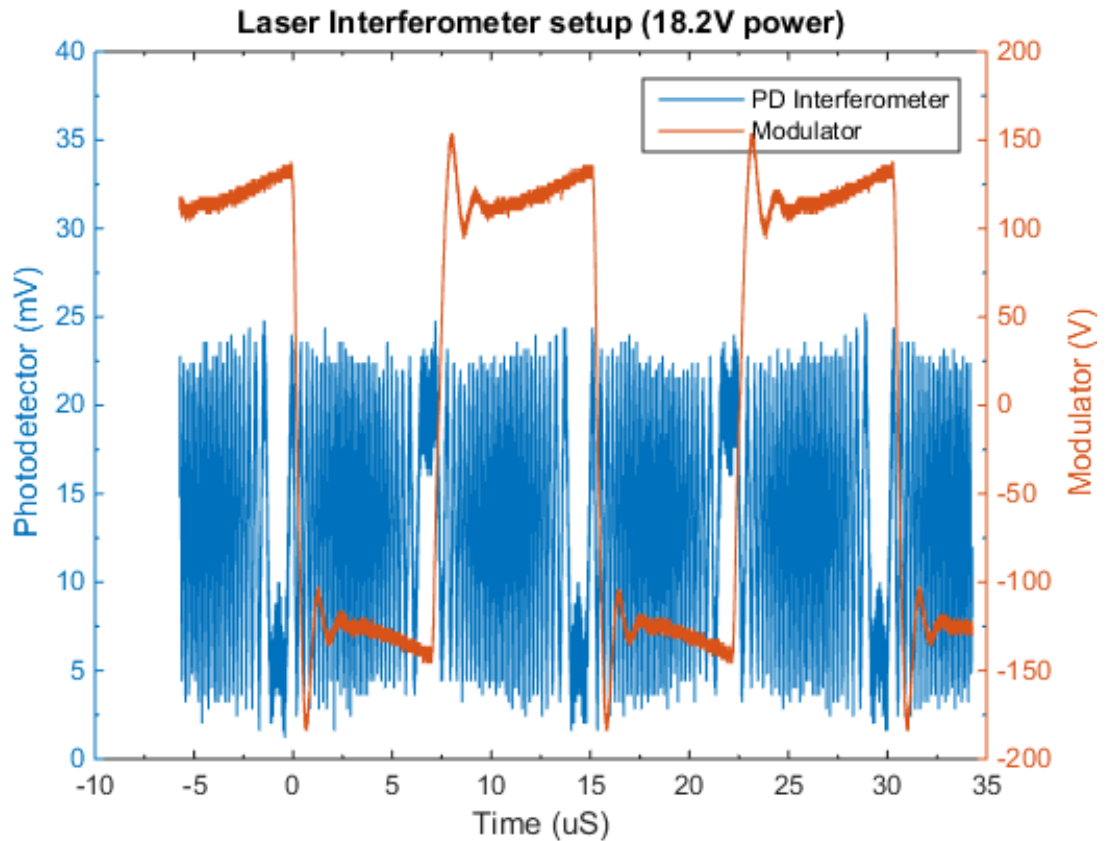
Figure 4-9: Sample capture from Tektronix MSO 4054 Mixed Signal Oscilloscope. The number of peaks in a cycle corresponding to the modulator cycle determines the displacement.

When power is increased, the mirrored face of the photoelastic modulator travels farther and thus generates a larger number of periods in the interferometer per period of modulator. The graphs on Figure 4-7, Figure 4-8, and Figure 4-9 are provided to show the progression in increase of number of periods which is what is used to generate the graph in Figure 4-10.

45
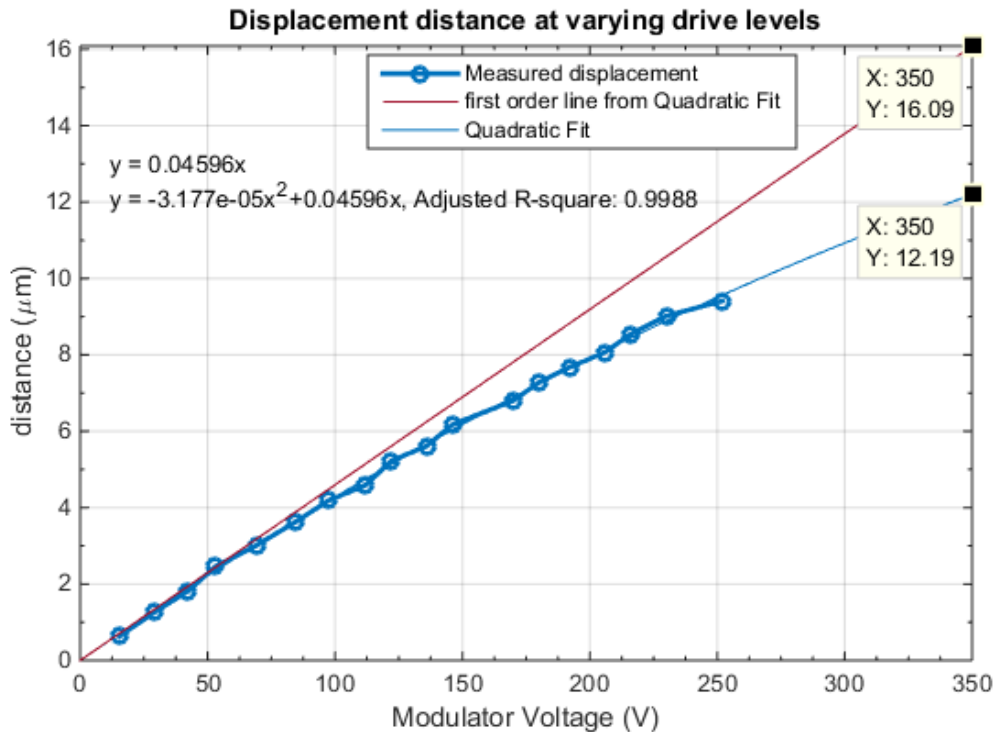
Figure 4-10: Measured displacement for a given modulator voltage V_{high}(avg)-V_{low}(avg) with both a quadratic line fit and a line from the first term of the quadratic fit.

It has to be assumed that the modulator is operating in its elastic range and thus its displacement for a given amount of input energy is linear. Fused silica is a brittle material like glass, and so like glass does not undergo plastic deformation before failing. However the measured displacement due to voltage is not linear, so it must be assumed that the energy lost at higher displacements is instead transformed into heat from the fused silica's internal friction.[43] The amount of displacement for a 350 volt drive, which was previously used, can be estimated to be +/-6.1µm or a total distance of 12.19µm. Previously another experiment was carried out where the fused silica was compressed. The calculated amount of displacement for full modulation in that experiment was 13.20µm. This is a close match to what was calculated in the analysis of modulation. The Young's modulus is calculated from the linear component of the model. The quadratic fit is used on the measurements to model nonlinear effects, the zeroth order term is not included in the model due to the fact that a displacement of zero should be assumed when the modulator is unpowered, i.e. zero modulator voltage. The

line then must cross the origin. The slope of displacement to modulator voltage is 4.6e-8m/V, and using previous results the Young's modulus can be determined.

$$\frac{\Delta L}{V_{mod}} = 4.6 * 10^{-8} \frac{m}{V} \tag{4-5}$$

$$\frac{V_{umpd}}{V_{mod}} = 5.77e^-3 \tag{4-6}$$

$$\frac{V_{umpd}}{F} = 4.80 * 10^{-4} \frac{V}{N} \tag{4-7}$$

$$\frac{F}{\Delta L} = 2.61 * 10^8 \frac{N}{m} \tag{4-8}$$

$$F = \frac{EA_0 \Delta L}{L_0} \tag{4-9}$$

$$E = \frac{F}{\Delta L} \frac{L_0}{A_0} = 58.5 * 10^{10} Pa \tag{4-10}$$

The Young's modulus is calculated to be 58.5 GPa verses the 71.7 GPa used in the initial calculations. This is about 18% off from the initial calculations which are assumed to be correct. However, the Young's modulus calculated from a linear fit of the data was very close to 71 GPa.

4.3 Displacement of Modulator in face normal to the Y-axis

The displacement of the face normal to the Y-axis shows the stress along the FS. Though the nodes of the PEM have zero displacement, the nodes are the regions of maximum stress. The pressure then causes the surface on the sides of the FS to bulge and sink in. It is expected that the maximum amount of displacement should occur in center of the FS.
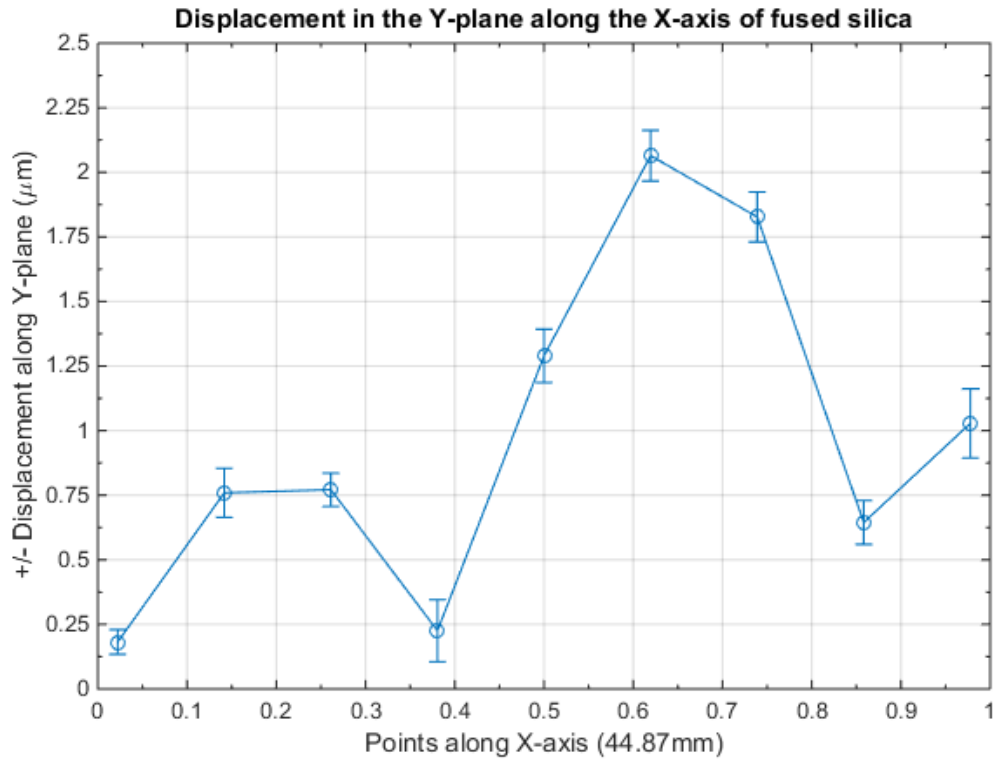
Figure 4-11: Displacement measured along the polished face of the fused silica. Each of the nine points has had their displacement measured ten times, the average is plotted, 'O' along with error bars.

Ten measurements at each point were combined to form the mean and standard deviation. Each of the nine points are equally spaced 5.36mm apart along the Y axis, centered along the Z axis, and with the first and last points one millimeter away from the ends of the FS along the X axis.

The PEM is first placed so that the laser beam is at a measurement point and then rotated on the Z plane so that the beam reflects back (vertical alignment). The laser beam is further aligned with the two micrometric mirrors so that an interference pattern is produced; typically this is done with a vertical alignment. The photo-detector is then visually aligned, first vertically then horizontally to the center of the interference pattern. The setup is checked for alignment by advancing the movable mirror (mirror 2 in Figure 4-6) via the linear actuator. A large signal implies large contrast which is a good indication of proper alignment. The generator was supplied with ten volts and the number of photo-detector signal cycles that occur within one generator cycle was

recorded, along with the location of the measurement point. The displacement is then calculated from the ratio of cycles from the photo-detector and the cycles from the generator and shown in Figure 4-11.

The maximum displacement occurs at 65% of the total length and a smaller hump is observed on the left at about 20% of the total length of fused silica.

The simulation done on COMSOL multiphysics, presented in Chapter 8, expects the offset of the maximum displacement away from the center of the fused silica as well as the slight rise in displacement on the right side of the PEM. The simulation predicted that there will be another maximum of displacement in the piezoelectric quartz which extends through the left side of the fused silica.
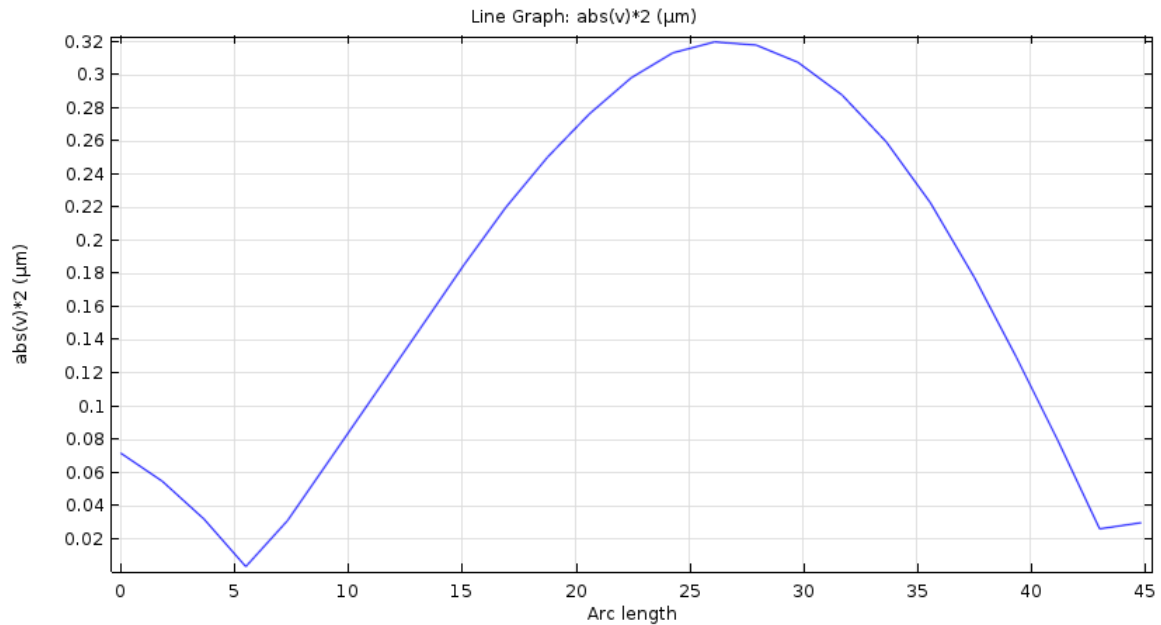
Figure 4-12: Comsol simulation of displacement in fused silica.

This however is not what is seen; the displacement drops off on the left side close to the interface between the two quartz and so forms a small hump on the left side. We can however assume that the locations along the X axis of maximum displacement in the Y-Plane denote the places of maximum stress. The conclusion is that the maximum stress location may not occur at the center of the fused silica but assumed to be offset 6.75 mm from the center due to a mismatch between the FS and Quartz.

Chapter 5   Comsol simulation

Comsol is a finite element analysis solver and simulation software. The application was chosen for its inclusion of piezoelectric physics modeling with solid mechanics modeling. Due to our inexperience with comsol, we've decided to first model each element of the PEM separately to first verify that the models are set up correctly. The simulation should give us some insight on the workings of the PEM, suggest improvements as well as diagnose problems and clear up misconceptions.

The model's physical dimensions are measured directly from the physical PEM. The piezoelectric actuator is first modeled and an eigen-frequency study performed so a resonant frequency which has maximum displacement of the face which attached to the fused silica is found i.e. an extensional mode. A frequency domain study is repeated over the same frequency so the response of the piezoelectric quartz to a sine wave with the resonant frequency and a magnitude of 350V is calculated. The piezoelectric quartz is included in comsol, we simulate it with Quartz RH (1978 IEEE). The density is close to what has been measured. Quartz RH density is 2651Kg/m^3 and the density from measurements of dimensions and weight is 2641.4 Kg/m^3. The other parameters of piezoelectric quartz have not been measured. It has been assumed that the piezoelectric quartz is x cut. Therefore the orientation of the crystalline axis in the actuator (piezoelectric quartz) should be trivial.
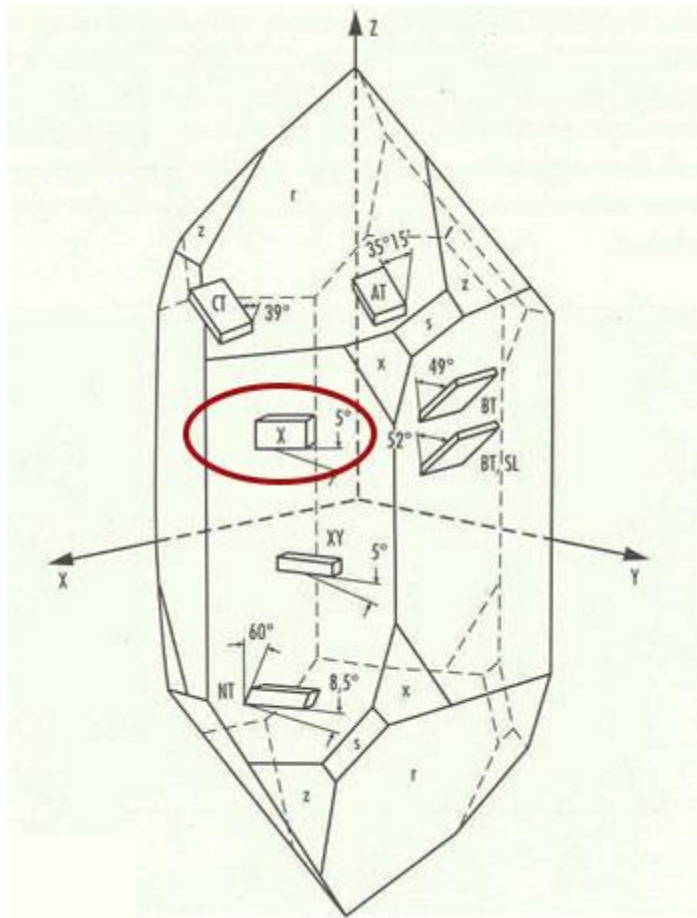
Figure 5-1: angle of cuts, X cut is circled in red. [44]
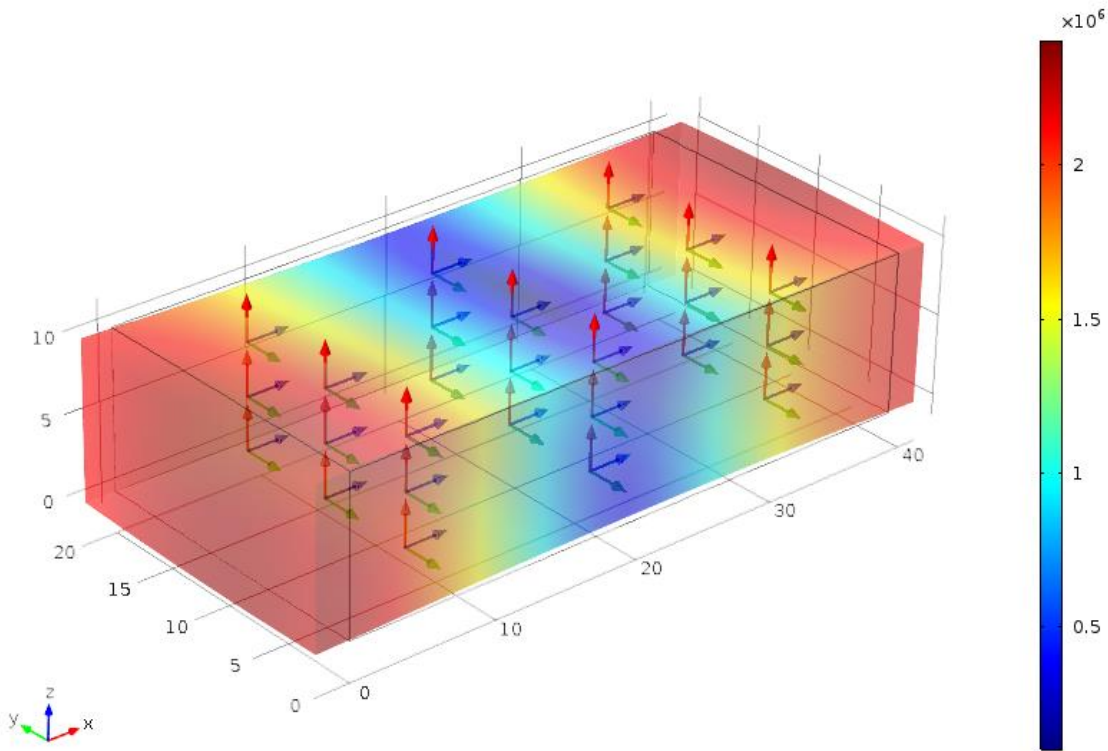
Figure 5-2: Shows the crystalline coordinate system which is rotated with respect to the local coordinate system.

Comsol has a built-in material, Quartz RH (1978 IEEE), which is used in the simulation. The 1978 IEEE standard defines the quartz material properties and the axis and is the most recent standard. The following properties of the material are of interest in the simulation:

Density- mass per unit volume

Elasticity matrix-anisotropic elasticity which describes how the solid deforms and stresses due to loading

Coupling matrix-couples the strain to the electric field

Relative permittivity- electric flux per unit charge in the material

Mechanical damping can be added later to model losses in the system due to non-idealities and loss due to the visco-acoustic coupling to air.

The coupling between structural and electrical domains is here expressed as a connection between the material stress and the permittivity at constant stress. The stress-charge form (e-form) and the relations are as follows:

$$\text{T} = c_E S + e^T E = 0.017\ pF \tag{5-1}$$

$$\text{D} = eS + \varepsilon_0 \varepsilon_{rs} E \tag{5-2}$$

Where:

c_E-material stiffness

e-Coupling properties

ε_{rs}-relative permittivity at constant strain

ε_0-permittivity of free space

T-stress

S-strain

E-electric field

D-electric displacement field

The elasticity matrix is highly symmetric due to physical reasons and thus it is written in COMSOL in an abbreviated form (Voigt notation). The full matrix is written below in Table 5-1.

Table 5-1: Elasticity Matrix for piezoelectric quartz (Quartz RH (1978 IEEE)

8.67E+10	6.99E+09	1.19E+10	1.79E+10	0	0
6.99E+09	8.67E+10	1.19E+10	-1.79E+10	0	0
1.19E+10	1.19E+10	1.07E+11	0	0	0
1.79E+10	-1.79E+10	0	5.79E+10	0	0
0	0	0	0	5.79E+10	1.79E+10
0	0	0	0	1.79E+10	3.99E+10

5.1 COMSOL simulation of matching quartz and FS

The comsol simulation was first run with the typical Young's modulus of FS and varying the dimensions of the quartz and FS such that both have the same resonant frequency.
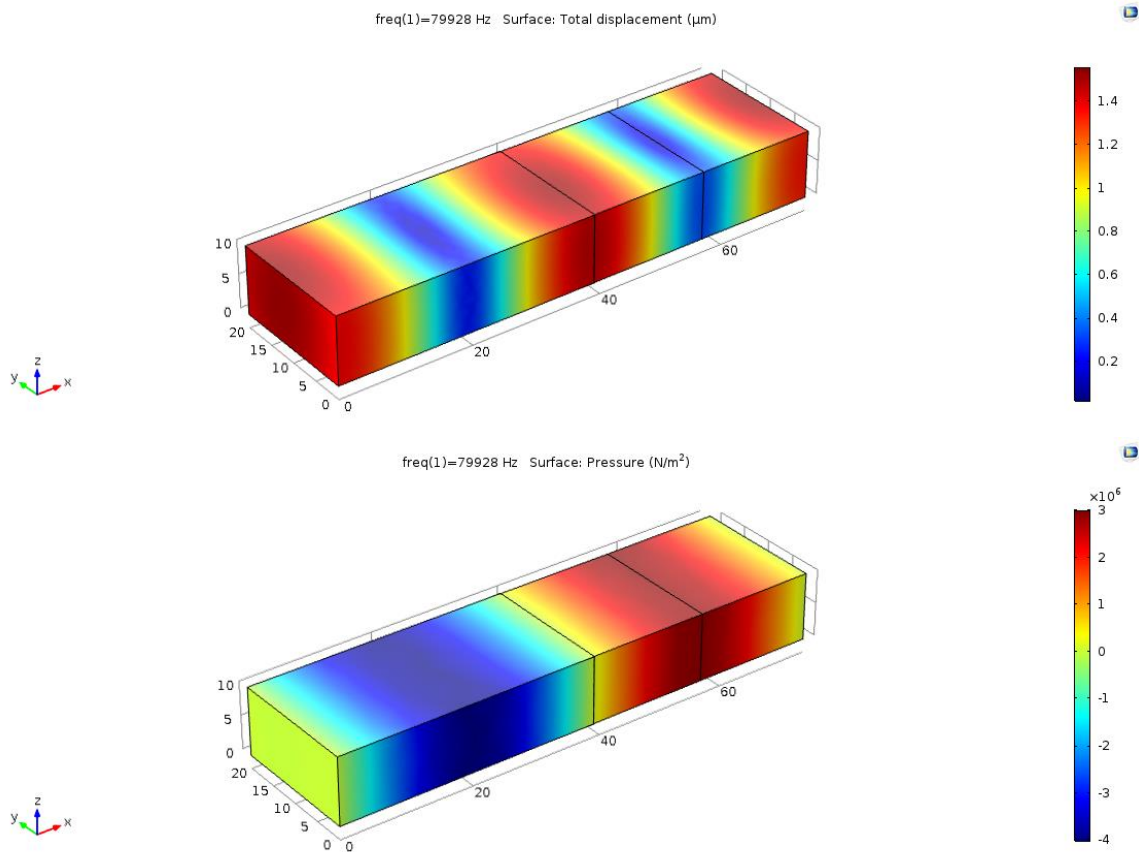
Figure 5-3: 3D Displacement and Stress with fused silica at 35.4715 mm resonance matched to COMSOL Quartz RH (1978 IEEE).

Figure 5-3 shows the result of simulation where the resonance of both piezoelectric quartz and fused silica are matched. The majority of displacement occurs on the two opposing faces and on the interface between piezo-electric quartz and fused silica, and minimal displacement in the middle of the components. The minimal displacement areas correspond with the nodes of the vibrational mode which also corresponds to the areas of concentrated stress.
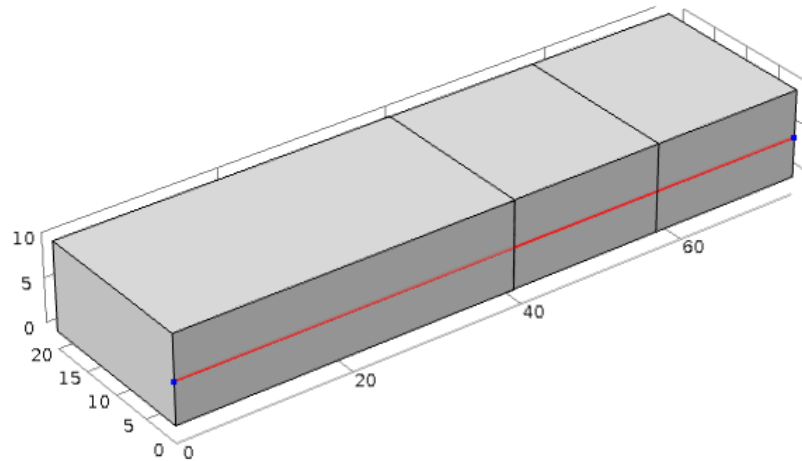
Figure 5-4: Cut line in 3D model where displacement in the Y direction will be measured along X.
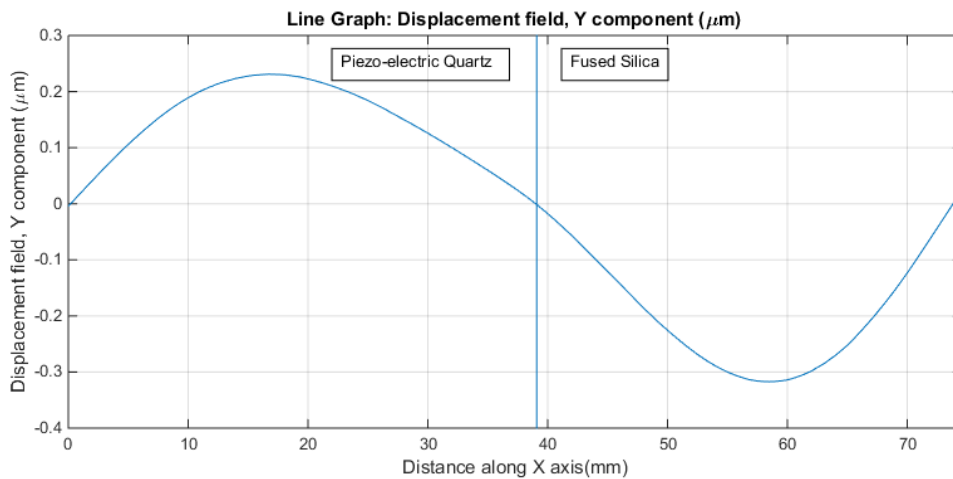
Figure 5-5: Y component of displacement along X, Arc length is in mm.

The smaller displacement of the PEM in the Y axis on a cut-line across the y face along the x axis was also collected in the simulation result. However, it reasonable to think that stress and the total displacement are inversely proportional. The reality is that the displacement-stress relationship is determined by the Poisson's ratio and that here the stress and the Y component of displacement are proportional, see Figure 5-8. Since there is an X component in the displacement as well, we can assume that the surface may tilt while it shifts back and forth. The consequence would be a small shift in angle of

55

the returning laser light which might affect accuracy of the displacement measurement especially in certain regions of the modulator face.

5.2 COMSOL simulation of quartz and FS

After simulating a modulator with matching fused silica, we model the modulator with the same parameters as the actual physical modulator.

freq(1)=71754 Hz Surface: Total displacement (µm)

freq(1)=71754 Hz Surface: Pressure (N/m^2)
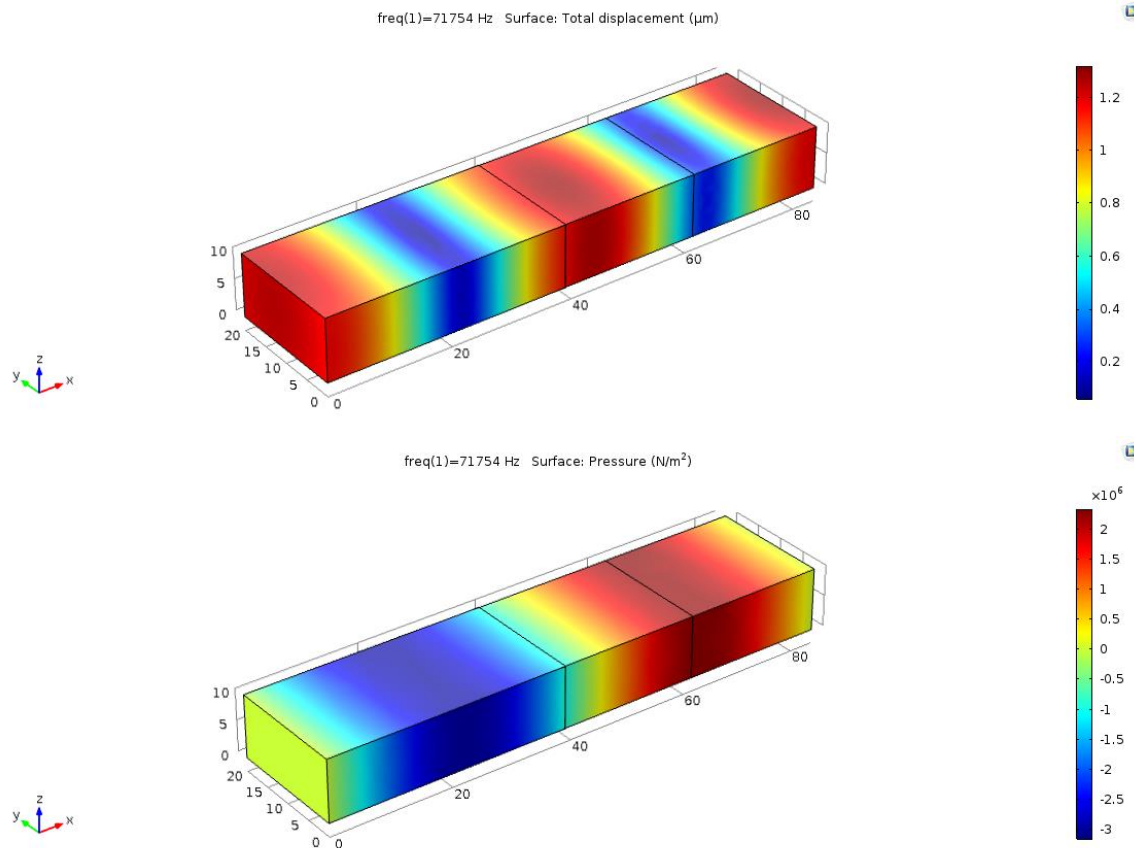
Figure 5-6: Figure 3: 3D Displacement and Stress with fused silica at 44.87 mm (actual)

The simulation shows that a miss-matched piezoelectric quartz and fused silica modulator has a shifted node offset from the interface region. In the assembly of the modulator, the FS and piezoelectric quartz are bonded with two part epoxy glue in that region. This means that the glue interface experiences stress that exceeds bond strength or may heat from repeated stress and delaminate. In addition, the area we assume to have the most stress and is used for modulating light is shifted away from the center of the fused silica.
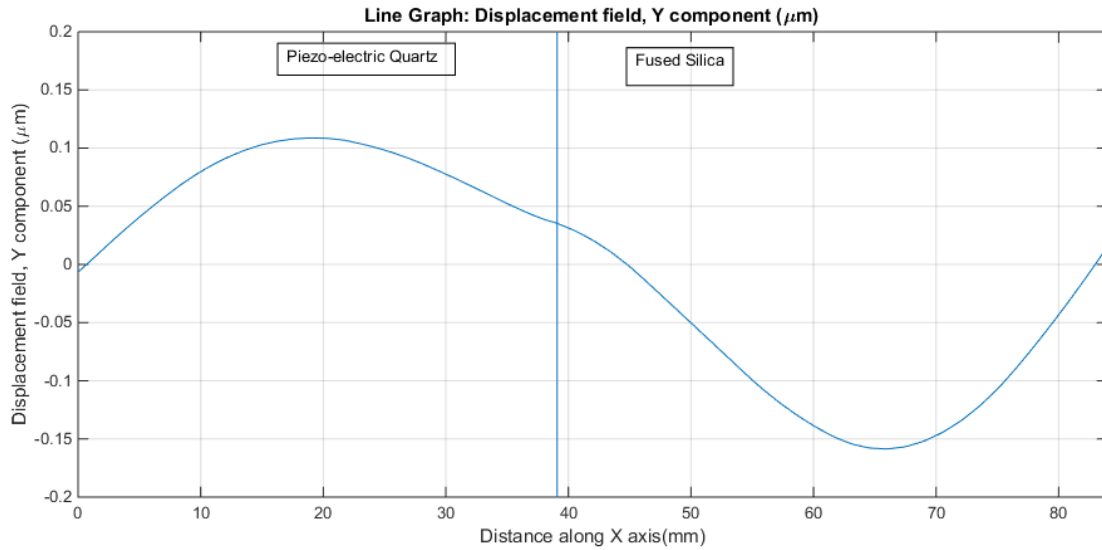
Figure 5-7: Y component of displacement along X in an unmatched Modulator
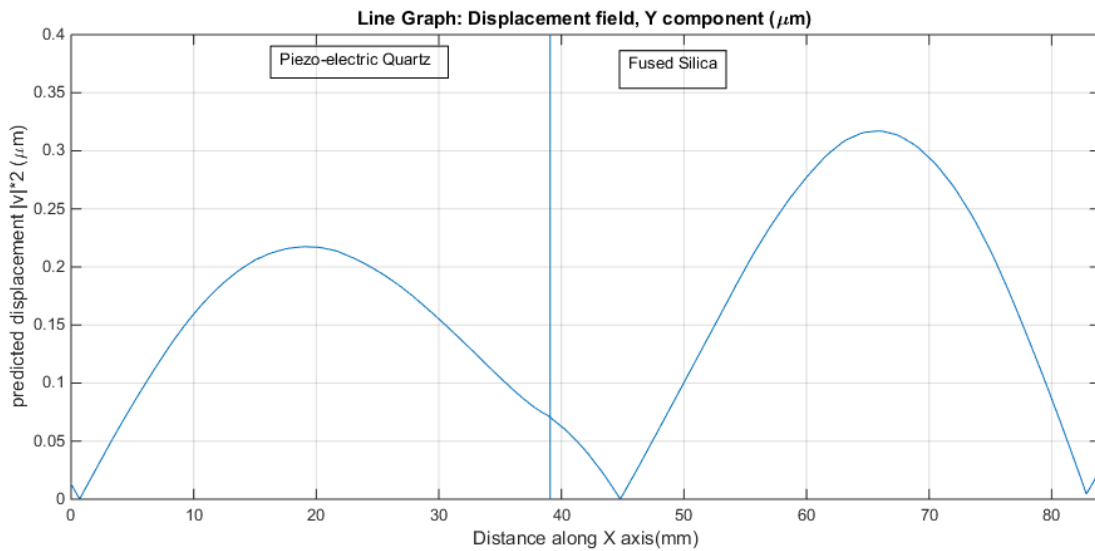
Figure 5-8: Predicted shape of displacement measured by interferometer setup.

The results of simulation (Figure 5-7 and Figure 5-8) show displacement in the Y axis where the two resonant frequencies of the constituents of the modulator are miss-matched. When compared with the results of an experiment performed at the end of section 4.3 seen as Figure 4-12, the displacement shown here in Figure 5-7 matches more closely to Figure 4-12 than the displacement shown in Figure 5-5 which points to signs of mismatch in the PEM.

The fused silica block resonance mode has both been calculated and also simulated in comsol. The results of calculation for resonance are as follows for the experimental FS block.

Table 5-2: Modulator parameters

	Piezo quartz	Fused Silica
X (mm)	39.08	44.87
Y (mm)	20.08	19.97
Z (mm)	10.03	10.03
Mass (Kg)	2.08E-02	1.97E-02
Density (Kg/m^3)	2641.41	2188.28
Young's Modulus (Pa)		7.17E+10
Poisson ratio		0.17

Speed of sound in a solid (long beam):

$$C_{solid} = \sqrt{\frac{Y}{\rho}}, l = n\frac{\lambda}{2}, f = \frac{c}{\lambda}, \frac{c}{2f} = l \qquad (5\text{-}3)$$

C- speed of sound

Y- Young's modulus

ρ-density

l-length

λ-wavelength

f-frequency

$$f = \frac{1}{2l}\sqrt{\frac{Y}{\rho}} \qquad (5\text{-}4)$$

$$(5\text{-}5)$$

$$f = \frac{1}{2*45.17mm}\sqrt{\frac{7.2*10^{10}Pa}{1.9667*\dfrac{10^{-2}kg}{19.97mm*44.87mm*10.03mm}}}$$

$$f \approx 63.79kHz$$

f-fundamental frequency, l-length of fused silica, Y-Youngs modulus, ρ-density

The Equation above (5-4) for finding the fundamental frequency does not take into account the Poisson's ratio which would have been used if the FS dimensions were larger than the wavelength and was adopted from calculating the speed of sound in long narrow beams(5-3); a beam that's diameter is shorter than a wavelength.

$$(5\text{-}6)$$

$$C_{solid,p} = \sqrt{\frac{E(1-v)}{\rho(1+v)(1-2v)}}, l = n\frac{\lambda}{2}, f = \frac{c}{\lambda}, \frac{c}{2f} = l$$

$$(5\text{-}7)$$

$$f = \frac{1}{2l}\sqrt{\frac{E(1-v)}{\rho(1+v)(1-2v)}} \approx 66kHz$$

f-fundamental frequency

l-length of fused silica

E-Youngs modulus

v-Poisson's ratio

ρ-density

   The speed of sound in a beam whose diameter is longer than a single wavelength takes into account the Poisson's ratio and is calculated above. A third source of data comes from Comsol which predicted the resonant frequency to be 63.393 kHz.

# Chapter 6   Resonant Frequency of Fused Silica bar

An experiment was performed to measure the resonant frequency. The goal of the experiment was to find the mode of oscillation with minimal error or offset. This will require that the fused silica be minimally loaded. Though the resonance frequency was predicted in the previous sections; this experiment would offer data from another approach and thus give more confidence in our previous measurements. As the FS should be minimally loaded, the piezoelectric quartz would not be attached and only the fused silica parameter would be measured. Inspiration to perform this type of measurement comes from a paper published in 1969. In 'Piezo-Optical Birefringence Modulators: New Use for a Long-Known Effect' an experimental electromagnetic drive system was described in which foil was Duco cemented to a bar. The following experiment attempts to duplicate the study.[45]

In the paper, the frequency was measured using single turns of aluminum wire bonded to the 'fused silica bar' with silicone rubber cement. The ends are placed into the magnetic fields of permanent magnets. This arrangement is not mechanically efficient but its merits are the low loads, creating what can be called a virtually unperturbed single element resonator. The setup then has one loop drive oscillations and the other as the positive feedback into the oscillator loop. The experiment performed however, deviates from the one described in the original source on some points. Instead of a feedback loop, one loop is driven by a frequency generator which is swept across a range of frequency and the other loop is used as a pickup and the amplified response is plotted. The number of turns was increased from just one turn in the hope that the system efficiency could be improved.

Magnet wires were first wound into flat coils with approximately ten turns and superglued to the ends of the fused silica bar; the coils have resistances of around one ohm. The assembly was supported and balanced on a double sided foam adhesive strip

60

across the center and two powerful neodymium permanent magnets placed on either side opposite the coils.

A driver circuit was built to supply one of the coils with high current AC voltage the input of which is a waveform generator, OWON AG1022. The other coil was used as a pickup, and its output was amplified around 1000 times and captured by the Tektronix

Coils
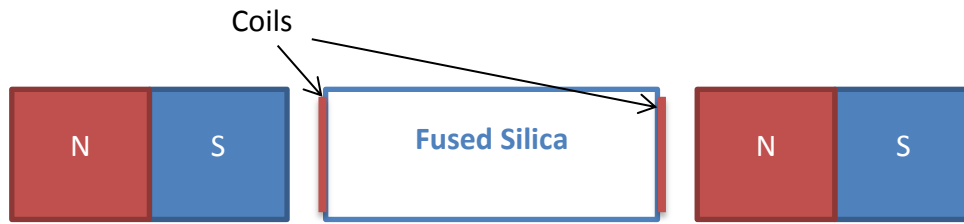
| N | S | | Fused Silica | | N | S |

MSO 4054 oscilloscope. The frequency is incremented, the process repeated and the result plotted in Figure 6-2.

Figure 6-1: Experimental setup

The driving coil induces vibrations in the fused silica which acts as a mechanical frequency filter. The FS mechanically vibrates and the signal is picked up by the second coil, the modal frequencies, which correspond to the resonant frequencies, however have a larger response. The response then should have a peak at resonance with a FWHM (full width half maximum) defined by its quality factor.
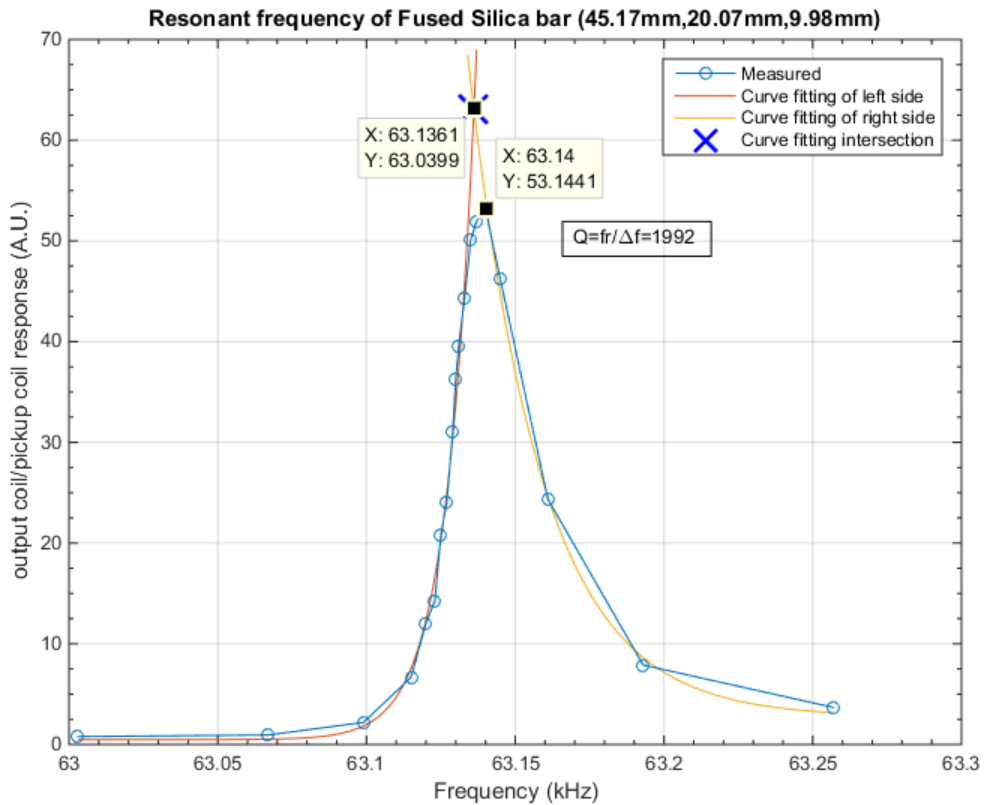
Figure 6-2: Output coil response.

The results show that the resonant frequency lies close to the calculated resonant frequency which confirms that the young's modulus of fused silica (FS) calculated from previous experiments can be used to predict the resonant frequency of the FS bar. The experiment also shows that the FS and piezoelectric quartz do not have matching resonant frequencies. The quartz resonates at 67.95 kHz. The FS oscillates slower than the piezoelectric quartz and therefore must be trimmed. The predicted length and frequency dependence is plotted below (Figure 6-3).
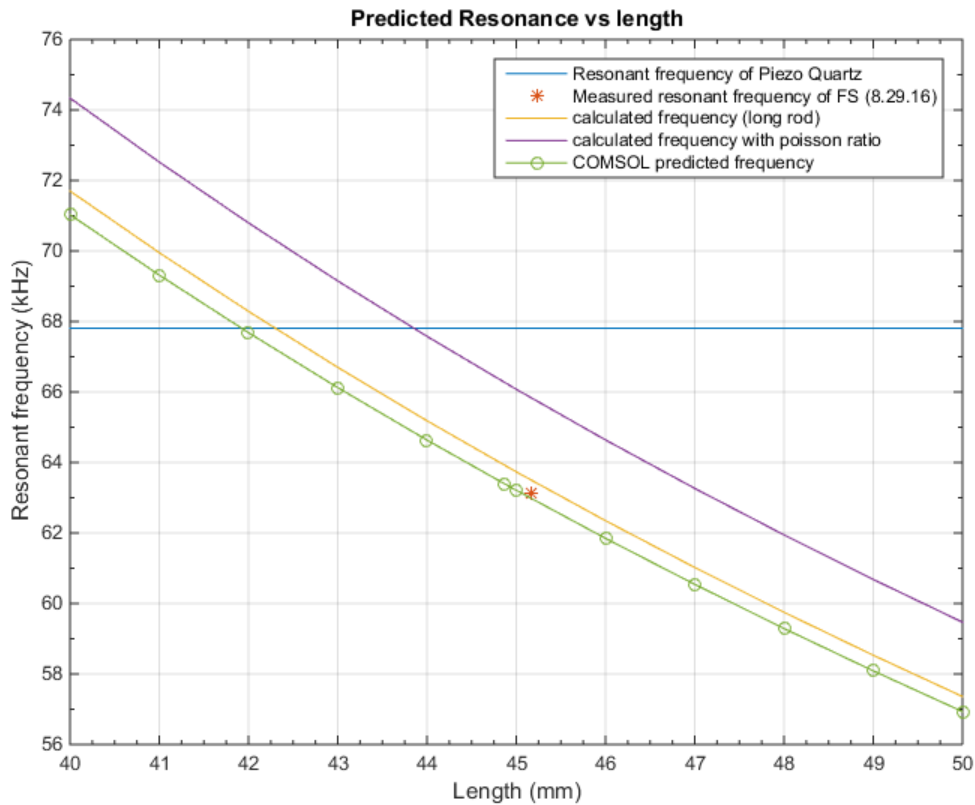
Figure 6-3: Calculated resonance frequency from FS bar length using several methods.

6.1   Conclusion

The result of this experiment (Figure 6-3) shows that the length and resonant frequency coincide with the predicted length to frequency with the exception of the calculated values taking into account Poisson's ratio (5-6),(5- (5-7). The reason for this is obvious, as it was stated that those calculations should be for beams whose diameter is longer than a wavelength. In our application the FS on its longest length should be half a wavelength and thus the FS width which is much shorter than its length would naturally be much less than one wavelength, and the equation with Poisson's ratio (5-6) should not be used.

6.2   Weight of coils compared to the weight of the FS

63

Concerns were raised, after the experiment was performed, about the effects of the added mass of the coils on the measured resonance frequency. Measuring the resonant frequency of the FS requires that there is minimal loading on the FS; therefore the coil mass should be only a small percentage of the total mass of the FS. The decision was made to measure the weight of the setup to determine the amount of loading from the coils.

The FS was weighed on a lab scale and the change in mass with the coils was measured.

Table 6-1: Change in weight of FS due to coils.

Total mass with pins, coils and wire, solder, and superglue	20.2454g
Mass of FS (45.17mm*9.98mm*20.07mm)	19.8525g
Mass of glue, coils and weight of half of the wires	0.0943g

The percentage of the coils and other added mass to the total FS setup is 0.47% and therefore should decrease the frequency measured by only a small amount. Generally the frequency change could be calculated if some other parameters of the materials used are known, but with such a minimal effect, it would not be justified.

Chapter 7   Impedance and RLC modeling

It is important to understand the modulators electrical model in order to mechanically drive the modulator. The typical four parameter model is presented and the resonant and anti-resonant frequencies are examined. The components of the model are then the electrical equivalent of the modulator which is calculated in the following section and is critical in the design of the oscillator circuit. The components of the passive circuit can also be equated to real physical attributes of the modulator. This type of analysis and modeling is typical and applies to most quartz crystals. We will use the standard model for a crystal and try to fit all the parameters to this model.[46] The resistance and reactance data to be fitted was first collected with the Quadtech 1920 Precision LCR Meter.
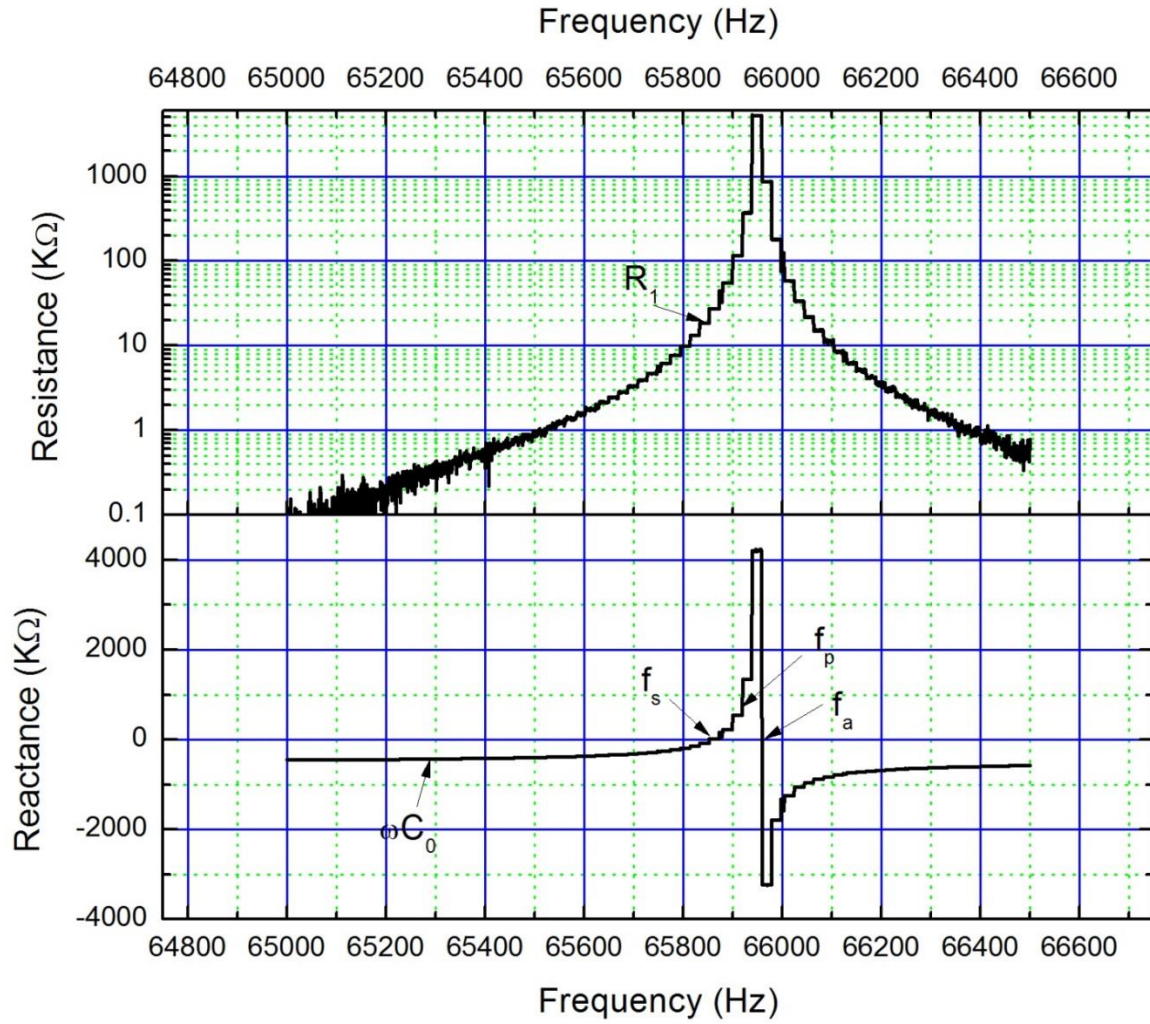
Figure 7-1: Plots of resistance, reactance of modulator.
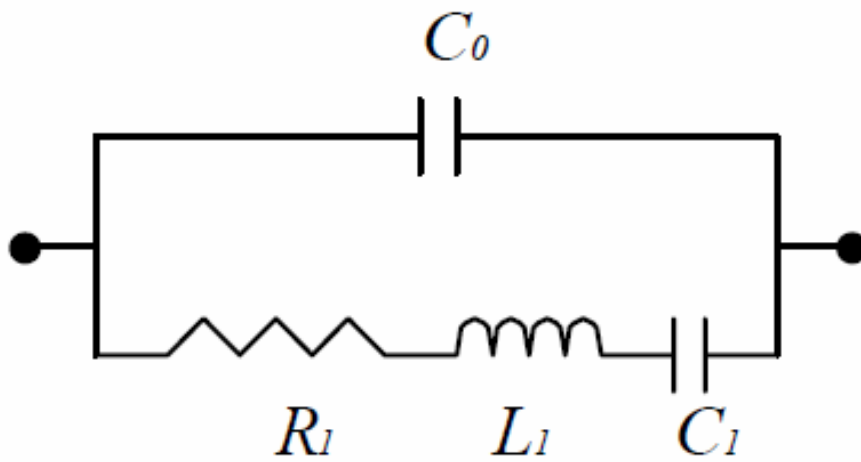
Figure 7-2: 4-parameter model of modulator.

C_0-Shunt Capacitance

C_1-Motional arm capacitance; actually represents the elasticity of the quartz.

L_1-Motional arm inductance, the vibrating mechanical mass of the quartz.

R_1- Resistive loss in crystal.

f_a- Anti-Resonance frequency.

f_s- Series Resonance frequency.

f_p- Parallel Resonance frequency.

Calculations of Crystal parameters:

$$f_s = 65.853 kHz, R_1 = 27.33 k\Omega$$

$$f_a = 65.958 kHz$$

$$X_s(at\ f\ far\ away\ from\ resonance = 65.09\ kHz) \approx 446.543\ k\Omega$$

$$X_s = \frac{1}{2\pi f C_0} \tag{7-1}$$

$$C_0 = \frac{1}{2\pi f X_s}, C_0 = \frac{1}{2\pi * 65.09 kHz * 446.543\ k\Omega} = 5.48\ pF \tag{7-2}$$

$$f_a = \frac{1}{2\pi \sqrt{L_1 \dfrac{C_1 C_0}{C_1 + C_0}}}, f_a = \frac{1}{2\pi \sqrt{L_1 C_1}}, f_a = f_s \sqrt{1 + \frac{C_1}{C_0}} \tag{7-3}$$

$$f_a = f_s \sqrt{1 + \frac{C_1}{C_0}}, C_1 = C_0 \left(\left(\frac{f_p}{f_s} \right)^2 - 1 \right) = 5.48\ pF \left(\left(\frac{65.958 kHz}{65.853 kHz} \right)^2 - 1 \right) \tag{7-4}$$

$$= 0.017\ pF$$

$$f_s = \frac{1}{2\pi \sqrt{L_1 C_1}}, L_1 = \frac{1}{C_1 (2\pi f_s)^2}, L_1 = \frac{1}{0.017 pF (2\pi * 65.853 kHz)^2} \tag{7-5}$$

$$= 344\ Henry$$

4

$$Q = \frac{1}{2\pi f_s R_1 C_1} = \frac{1}{2 * \pi * 65.853 kHz * 27.33 k\Omega * 0.017\ pF} = 5201 \qquad (7\text{-}6)$$
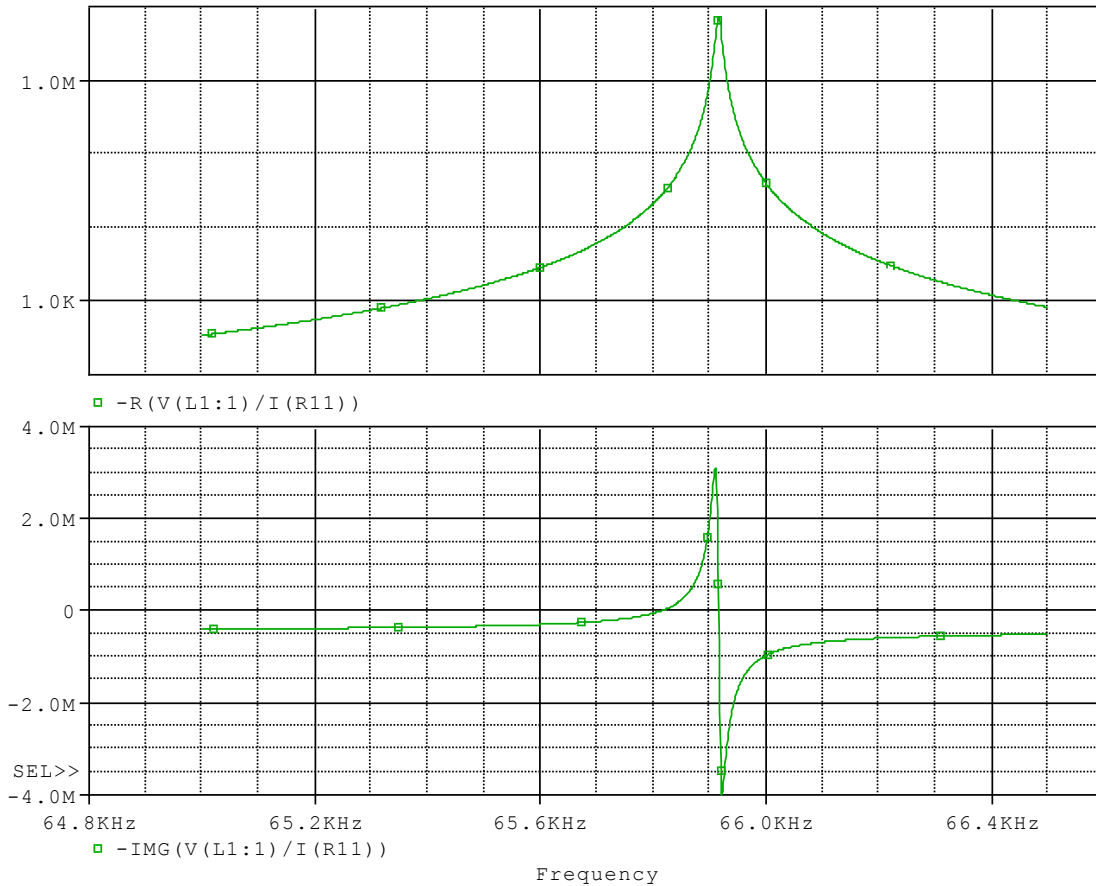
Figure 7-3: Simulation of Resistance, Reactance from calculated parameters

The electrical model is simulated and the plots shown in Figure 7-3 closely matches when compared to the original plots Figure 7-1 which suggests that model parameters matches the modulators. However there are other resonance modes, at least one such mode of oscillation occurs at a lower frequency than this. The high impedance X_S at low frequencies requires large gains in the amplifier as it is a source of gain loss. The parameters of the electrical model have a relationship to the physical attributes of the modulator. The inductance L_1 is based on the mass of the modulator. Capacitance C_1 arises from the stiffness of the modulator. R1 resistance is then the loss,

68

typically frictional loss from mechanical vibration. Shunt terminal capacitance C_0, is also considered to be part of the external load and affects the circuit accordingly and is based on the capacitance formed from the two terminal plates of the piezoelectric quartz portion of the modulator.

Chapter 8   Generator

The modulator requires high voltage AC with a frequency that matches its resonant frequency. The original design of the modulator used a ring oscillator operating at a frequency close to resonant frequency to start oscillations. The ring oscillator output is suppressed with a feedback signal through shunting via a mosfet. A signal, from the ring oscillator when output is not suppressed or from the modulator feedback when it exists, goes to a Mosfet driver then to power mosfets which in turn drives a custom transformer. The return path from the modulator consists of voltage limiting diodes which shunts excess current to ground. A feedback signal from this point is used to drive the circuit in resonant mode.

This system was improved to be robust against component variations in manufacturing. The move from hardware to software for some parameters of operations allows for faster, easier adjustments of operational parameters and intelligent monitoring/reporting of generator status. The choice was made to update the generator design to take advantage of advances in technology since the time it was developed.

The new generator circuit takes elements from the previous design. It uses the custom magnetics i.e. transformer of the original version and adds a microcontroller with built in comparators. A variable voltage switching step up converter was used to supply the correct voltage range for the mosfets to drive the transformer. The microcontroller attempts to start the process of resonant oscillations by first generating PWM signals to the MOSFETs and then switching the control to the comparators. If the frequency of oscillation is not correct (within certain parameters), the process starts again. This takes the role of the ring oscillator circuit with shunting. This occurs during the 'start-up' phase. The microcontroller indicates the current status through three

colored LEDs; Red - no resonance or lower frequency than expected, blue – resonance and normal operation, and green - higher frequency than expected.

8.1 Oscillator Theory
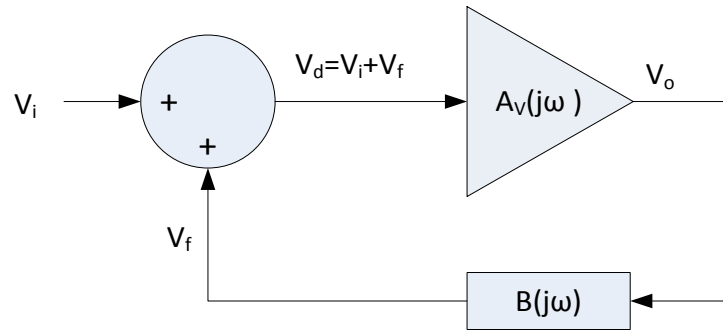
Figure 8-1: Basic feedback circuit[47]

V_i-external signal, whose source is typically noise which starts oscillation

V_f-feedback signal

V_d-sum of feedback and external signal

V_o-Voltage output

$A_v(j\omega)$-Amplifier voltage gain

$B(j\omega)$-Voltage feedback network

$$V_o = A_v(j\omega)V_d \tag{8-1}$$

$$V_f = \beta(j\omega)V_o \tag{8-2}$$

$$V_d = V_i + V_f \tag{8-3}$$

Then from Equation (8-1) to Equation (8-3) the closed loop voltage gain $A_{vf}(j\omega)$ is:

$$A_{vf}(j\omega) = \frac{V_o}{V_i} = \frac{A_v(j\omega)}{1 - \beta(j\omega)A_v(j\omega)} \tag{8-4}$$

Oscillations should occur and be sustained without any input, thus under steady state operation V_i is zero and so $\beta(j\omega)A_v(j\omega) = 1$. This is known as the Barkhausen stability criterion which states that steady state oscillations occur at frequencies where the loop

gain is unity and the phase shift is 2π. For oscillators that limit output by naturally saturating from the power rails as in our generator, gain may be greater than one, and must be greater than one for oscillations to grow to the steady state amplitudes.

A simplified schematic of the oscillator circuit is shown below.
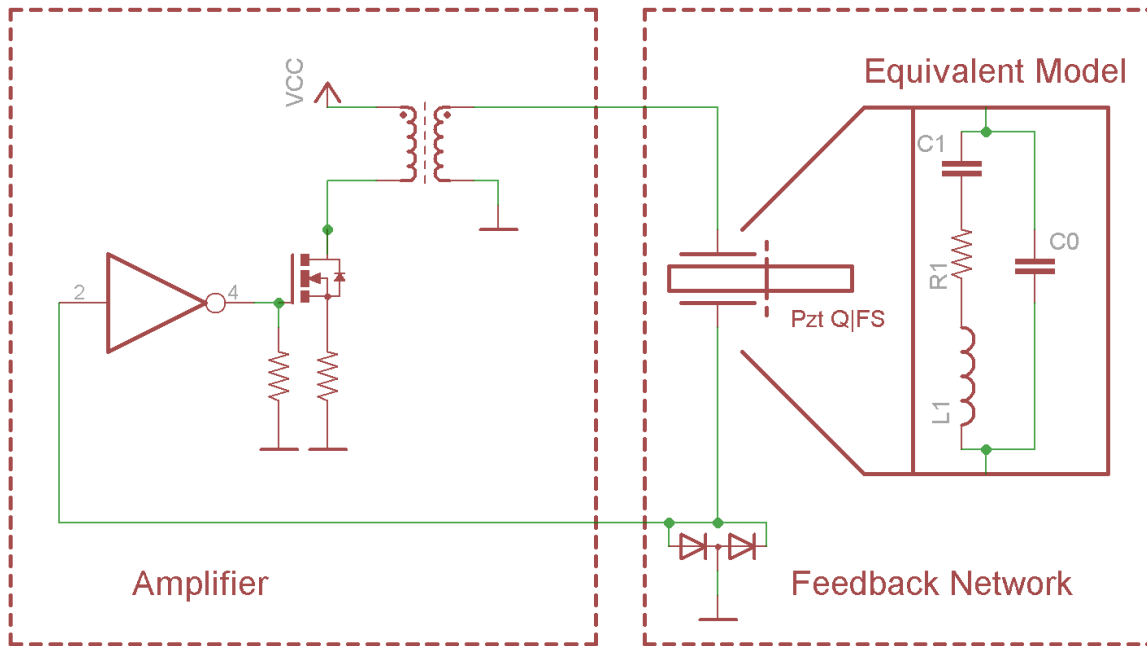
Figure 8-2: Simplified Schematic with equivalent model
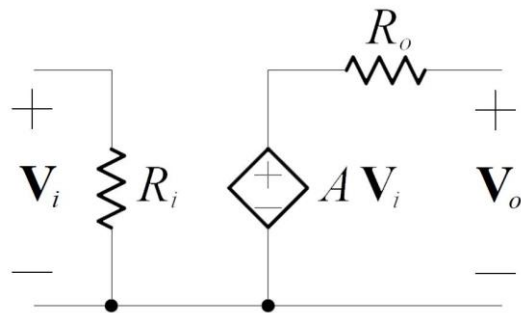
Figure 8-3: unilateral Open-Loop Amplifier
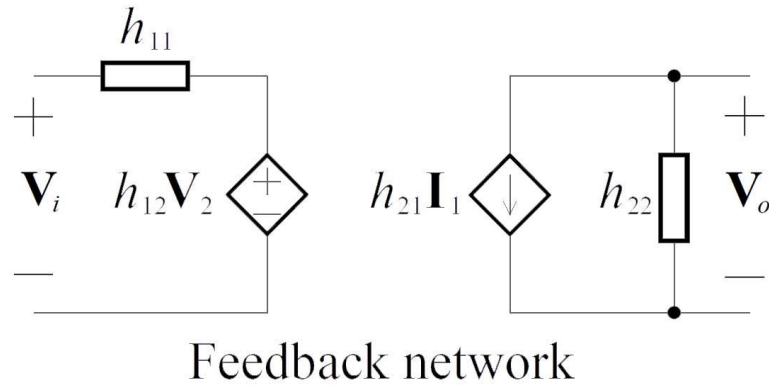
Figure 8-4: Ideal Voltage-sampling, voltage-mixing feedback network
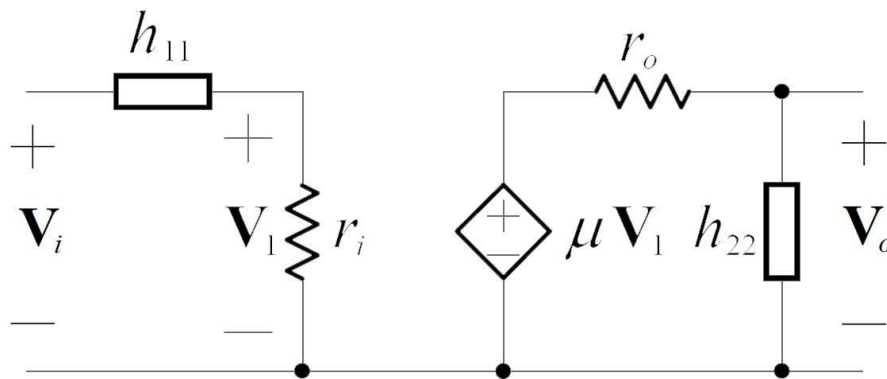
Figure 8-5: Thevenin equivalent of amplifier with h₁₁ and h₂₂ from feedback network.

From Figure (8-9):

$$R_i = h_{11} + r_i \tag{8-5}$$

$$R_o = r_o \parallel h_{22} \tag{8-6}$$

$$A = \frac{h_{22}}{h_{22} + r_o} \mu \frac{r_i}{r_i + h_{11}} \tag{8-7}$$

$$I_{out}(\lambda) = I_0 e^{-\alpha(\lambda)CL} \tag{8-8}$$
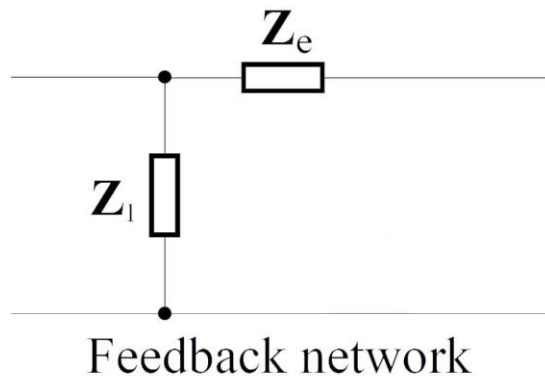
Figure 8-6: Feedback network with Quartz Oscillator (Z_e)

Using impedances from the feedback network:

$$h_{11} = Z_1 \parallel Z_e \tag{8-9}$$

$$h_{22} = Z_1 + Z_e \tag{8-10}$$

$$h_{12} = \frac{Z_1}{Z_1 + Z_e} \tag{8-11}$$

Then A from Equation (8-7) is:

$$A = \frac{Z_1 + Z_e}{Z_1 + Z_e + r_o} \mu \frac{r_i}{r_i + (Z_1 \parallel Z_e)} \tag{8-12}$$

And:

$$\beta = \frac{Z_1}{Z_1 + Z_e} \tag{8-13}$$

Some simplifications can be made to Equation (8-12), input resistance r_i for amplifiers is typically large $r_i = \infty$, so the h_{11} term can be dropped. Applying the effect from the large resistance, the loop gain is:

$$A\beta = \frac{Z_1}{Z_1 + Z_e + r_o} \mu \tag{8-14}$$

Let:

$$Z_1 = jX_1(\omega), Z_e = R_e + jX_e(\omega) \tag{8-15}$$

The loop gain is then:

$$A\beta = -\frac{X_1(\omega)}{X_1(\omega) + X_e(\omega) - j(R_e + r_o)}\mu \tag{8-16}$$

From the Barkhausen stability criterion, the imaginary part is zero and the gain is greater or equal to one at resonance.

$$R_e = -r_o \tag{8-17}$$

$$-\frac{X_1(\omega_0)}{X_1(\omega_0) + X_e(\omega_0)}\mu > 1 \tag{8-18}$$

$$\mu \le -(1 + \frac{X_e(\omega_0)}{X_1(\omega_0)}) \tag{8-19}$$

The power dissipated by the crystal can then be calculates as follows:

$$I_e = \frac{V_o}{R_e + j(X_e(\omega_0) + X_1(\omega_0))} \tag{8-20}$$

Where $R_e + jX_e(\omega_0)$ is the impedance of the piezoelectric quartz and is represented as:

$$R_e + j(X_e(\omega_0) = C_0 \parallel R_1 + L_1 + C_1$$

These are the parameters from Figure 7-2 of which the values were found in Equations (7-1) to (7-5).

At resonance, it is assumed that high voltage AC is applied to the terminal of the modulator, and as such the voltage limiting diodes are active, and the diodes are able to switch at higher frequencies than the resonance frequency. The voltage drops on the diodes are much smaller than the voltage applied and the impedance of Z_1 is small and real. Before the stable oscillation state however, the stray capacitance may play a small roll in X_1. For the imaginary portion to be zero, X_e must have an equally small inductive portion. This implies that the power dissipated on the modulator is:

$$P_{Modulator} = R_e|I_e|^2 \approx R_e \frac{|V_o|^2}{|R_e + j(X_e(\omega_0) + X_1(\omega_0)|^2} \tag{8-21}$$

It is obvious that the actual device is different than the simplified case; however this model gives insight to its operation and feedback criteria.

Nonlinear effects occur due to the saturation characteristics of the amplifier. We are using this configuration with the amplitude control performed by the supplied voltage. Typically noise voltage starts oscillation however the high impedance and high Q of the modulator means that the feedback gain is so low that the amplifier gain is not sufficient to satisfy the Barkhausen stability criterion, and any oscillations that do occur decays.
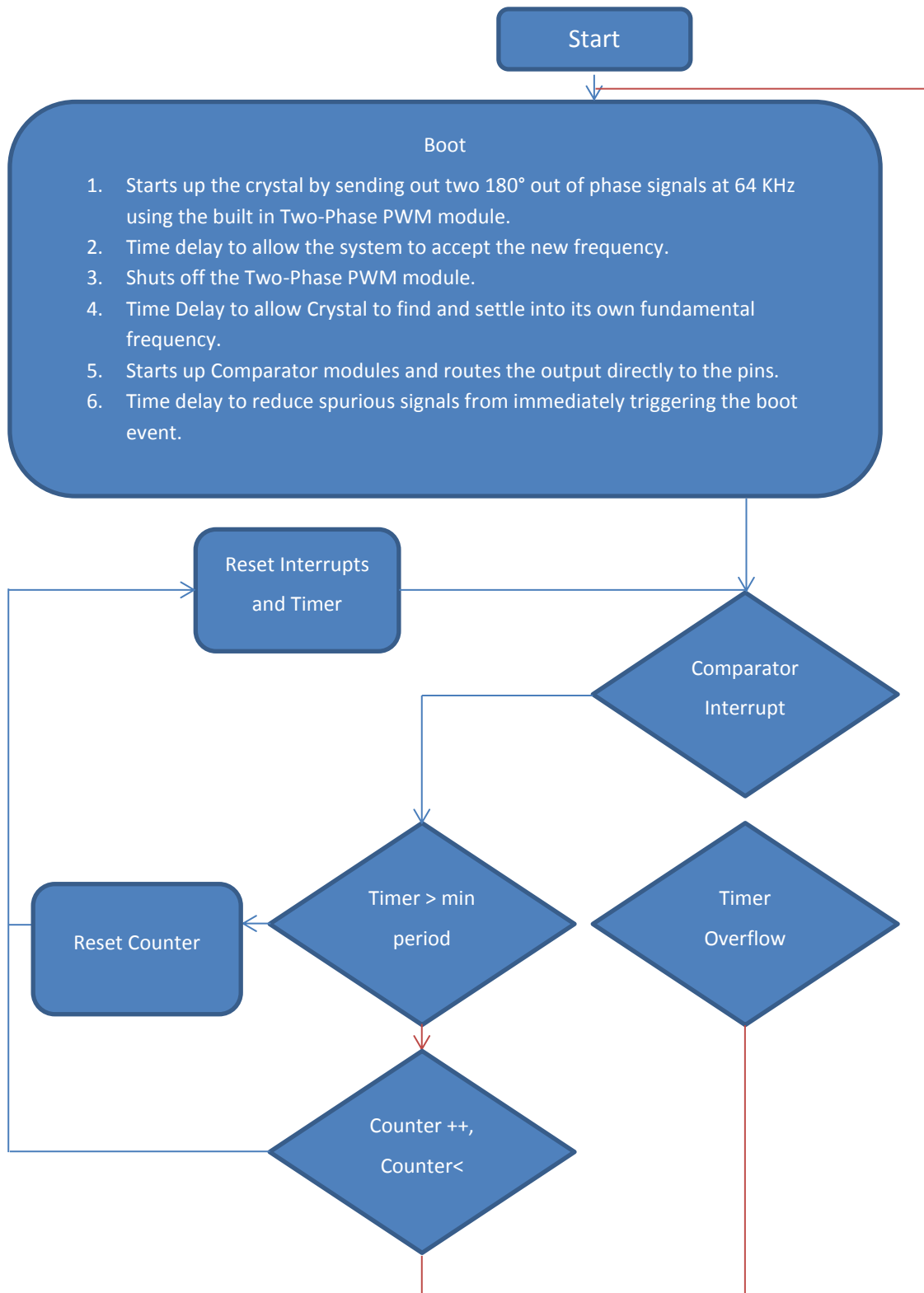
Figure 8-7: Flow chart of the microcontroller code.

The microcontroller, a PIC16F785 is used here to perform several tasks:

Monitoring- Monitoring of the oscillator is done with a high impedance input pin which allows the microcontroller to roughly estimate the frequency of oscillation and determine whether oscillations are within set boundaries.

Startup- The microcontroller switches to PWM mode where it outputs a drive signal to the mosfets. The timing of which is based on the internal oscillator of the microcontroller.

Restart- When the monitoring mode determines that oscillations are out of bounds, as in the case where oscillations cease, are too low or too fast, the microcontroller restarts oscillation through the startup task.

Feedback- Feedback is the normal operating condition of the system. The microcontroller configures one of its peripherals as an inverter and buffer to drive the mosfet with low latency. The PWM is shut off and the input and output pins are routed to the peripheral.

Communication- Communication of the status of the generator is done through I2C, a common communication protocol. In the future other parameters can be added: Powering voltage, time since last error, error type, startup frequency, startup time etc.

Indication- Three LED status lights are used to indicate the operational status of the generator; red, green and blue corresponds to lower frequency, higher frequency and correct operational frequency respectively.

The transfer function of the inverter in the system can be assumed to be stable across all frequencies till around its maximum switching frequency. As the modulator is attached serially in the feedback loop, the transfer function of the modulator thus dominates at the lower frequencies. This means that low frequency gain is small. The lack of filtering also means that any lower frequency poles which are encountered traps the system in that lower frequency. The kick start starts the system off at a frequency close to the pole associated with the resonant mode of the modulator where hopefully the system will stabilize and resonate at the correct frequency. The system then naturally increases gain as the feedback frequency approaches resonance due to the

modulator frequency response. But because the Q factor is high, resonance is narrow, therefore gain falls off rapidly at nearby frequencies. A high Q factor also reduces the total amount of energy transferred back through feedback and can hinder oscillation.[47]
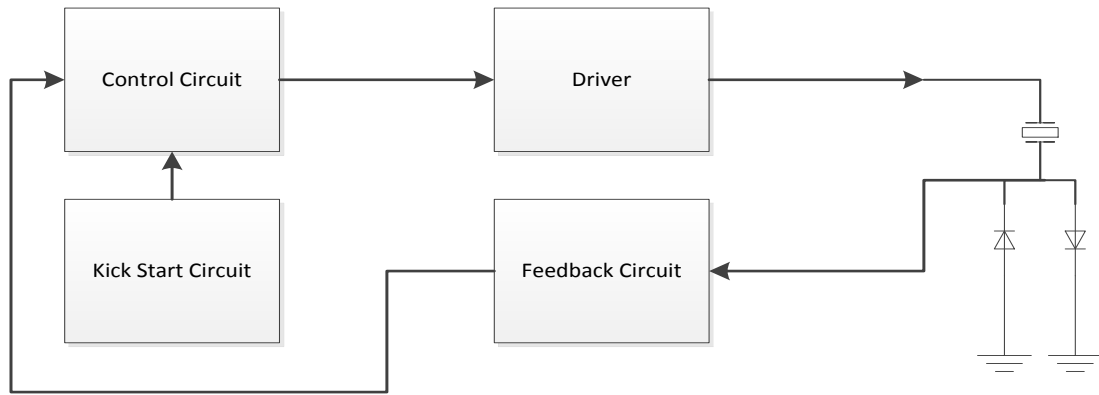
Figure 8-8: Block diagram of oscillator system consisting of generator and modulator
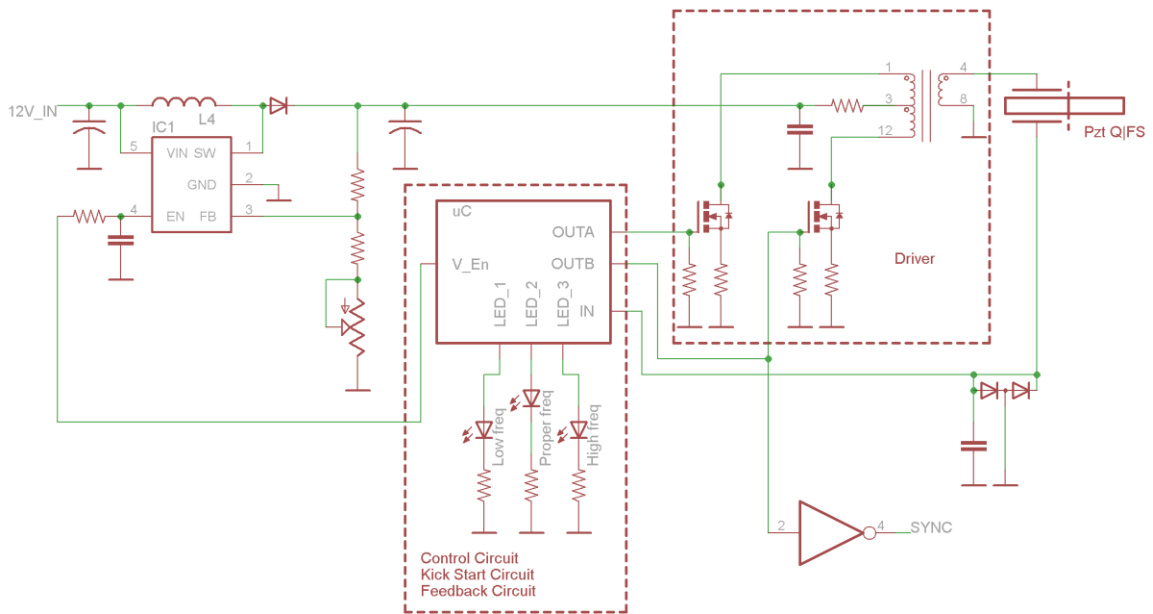
Figure 8-9: Simplified schematic of generator.
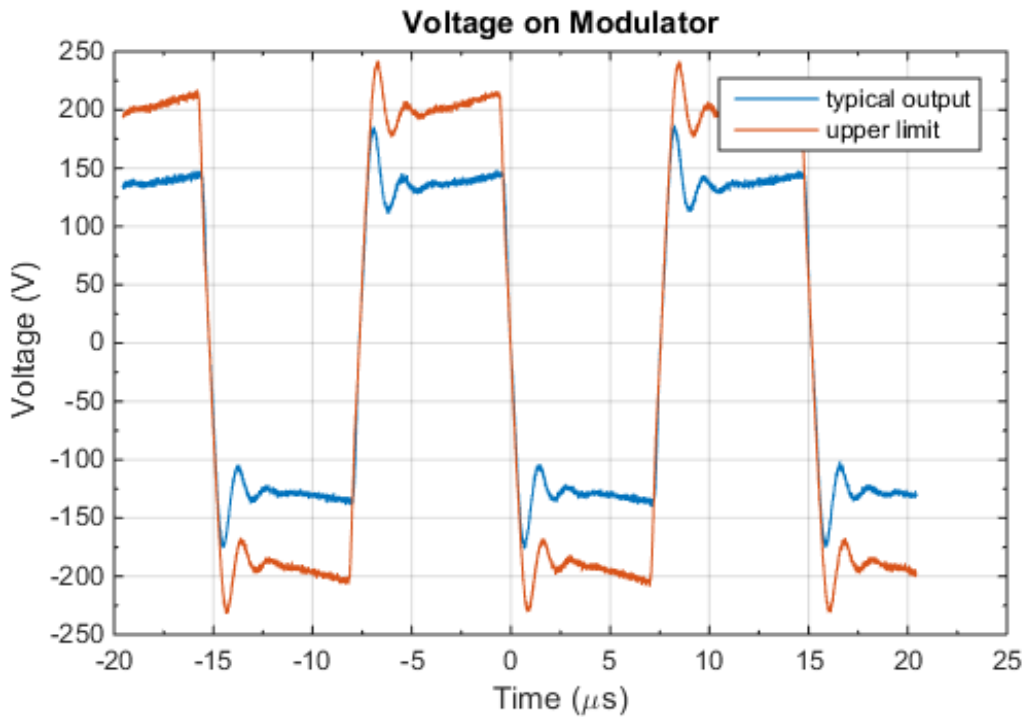
Figure 8-10: Output of the generator, adjustable via potentiometer.

8.2   Efficiency of new generator

The efficiency of the generator has been improved by substituting the inverter for a high speed comparator internal to the microcontroller with short switching times of ten nanoseconds and a propagation delay of less than 40 ns[48] and by removing the mosfet driver from the circuit. The results are as follows.

Table 8-1: Generator power consumption

	Voltage (V)	line	Current (A)	Power (W)
Original Generator	12	main	0.116	1.392
	5	digital	0.00183	0.00915
	-5	analog	0.002129	0.010645
Total Power				1.411795

Current Design	12	main	0.0854	1.0248
Total Power				1.0248

The cost of all components of the original generator excluding the transformer was $15.96 USD each for 100 units, the redesigned version costs $8.03 USD each for 100 units. The number of components has also been reduced from 56 to 35.

8.3 Generator conclusion

The generator stability and robustness has been improved as well as flexibility in performance over larger deviations in tolerances. The previous design utilized a ring oscillator of which the oscillation frequency was set by a resistor capacitor combination, when there are small variations in the resonant frequencies of the modulator the RC constant had to be changed manually, furthermore the shunting of the ring oscillator sometimes failed and the modulator would run continuously at the ring oscillator frequency. The cost per unit has been reduced from the previous design. However it is in the opinion of the author that more could be done in improvement of design. The analysis of the feedback path of the oscillator shows a path to a more robust redesign based purely on feedback. Another probable design could utilize a numerically controlled oscillator (NCO) to drive the modulator at resonance frequencies. These methods would be interesting to pursue as future work.

Chapter 9 Conclusion:

CH$_4$ detection is important, its uses widely ranges from industrial to medical and even to aerospace. CIPS fills an important niche in that it delivers very high sensitivity with high selectivity, detecting low levels of methane in the presence of other gases, and doing so quickly and relatively cheaply while also occupying a small footprint.

In this dissertation, CIPS and in particular cIPF (correlated interference polarization filter) is described in detail. The mathematical model of the PEM (photoelastic modulator) was derived and its drive was optimized for the best efficiency. The cIPF and the etalon were analyzed, and the signal seen with and without methane was presented.

Several methods to determine the Young's modulus and ultimately the optimal length of Fused Silica (FS) for resonance matching with the piezoelectric quartz were calculated for the PEM. COMSOL, a finite element solver, was used to simulate the operation of the PEM, generate predicted vibrational modes and determine the frequency of oscillations for varying lengths. This software package was used due to its multiphysics problem solving capabilities. The recommendation to change the geometry of the FS was finally concluded as evidence from several experimental approaches converges on a similar result.

The PEM's electrical model was determined and the oscillator circuit consisting of the modulator and generator was derived. The generator was redesigned to be more efficient, robust and its cost was reduced, while adding more features.

The future of this device is very promising, so far there have only been two real world applications which means the full potential of this technology has not been reached. Different types of hydrocarbon gases also exhibit fine spectral lines in the IR region; CIPS technology can be modified to detect these gases. The method of altering the polarization state does not need to be constrained to birefringence in FS. There are

many other techniques that can produce the same effect. Another potential direction for sensorCAT is work on the PEM. The PEM can also be made with piezoelectric ceramic instead to reduce cost and size. In this case, COMSOL would be a promising tool to simulate the assembly and aid in design.

References

1. Bedfont® Scientific Ltd. *Gastrolyzer*. Available from: http://www.bedfont.com/shop/gastrolyzer.

2. McKay, L.F., M. Eastwood, and W. Brydon, *Methane excretion in man--a study of breath, flatus, and faeces.* Gut, 1985. **26**(1): p. 69-74.

3. Lee, D.-D. and D.-S. Lee, *Environmental gas sensors.* IEEE Sensors Journal, 2001. **1**(3): p. 214-224.

4. Wong, J.Y. and R.L. Anderson, *Non-Dispersive Infrared Gas Measurement*. 2012: Ifsa Publishing.

5. Barsan, N. and U. Weimar, *Conduction model of metal oxide gas sensors.* Journal of Electroceramics, 2001. **7**(3): p. 143-167.

6. Wang, C., et al., *Metal oxide gas sensors: sensitivity and influencing factors.* Sensors, 2010. **10**(3): p. 2088-2106.

7. Davenport, J.W., *Ultraviolet photoionization cross sections for N 2 and CO.* Physical Review Letters, 1976. **36**(16): p. 945.

8. *Flame ionization detector*. 1968, Google Patents.

9. Jorgensen, A.D., K.C. Picel, and V.C. Stamoudis, *Prediction of gas chromatography flame ionization detector response factors from molecular structures.* Analytical Chemistry, 1990. **62**(7): p. 683-689.

10. Lee, J.H., J.H. HEO, and H.H. CHO, *Colormetric sensor detecting analytes with visual examination*. 2015, Google Patents.

11. Aroutiounian, V.M., *Hydrogen detectors.* Int. Sci. J. Altern. Energy Ecol, 2005. **3**: p. 21-31.

12. Han, C.-H., et al., *Synthesis of Pd or Pt/titanate nanotube and its application to catalytic type hydrogen gas sensor.* Sensors and Actuators B: Chemical, 2007. **128**(1): p. 320-325.

13. Ma, L.-S., et al., *Ultrasensitive frequency-modulation spectroscopy enhanced by a high-finesse optical cavity: theory and application to overtone transitions of C 2 H 2 and C 2 HD.* JOSA B, 1999. **16**(12): p. 2255-2268.

14. Zorabedian, P., *Tunable external-cavity semiconductor lasers.* Tunable Lasers Handbook, 1995: p. 349-442.

15. Cassidy, D.T. and J. Reid, *Atmospheric pressure monitoring of trace gases using tunable diode lasers.* Applied Optics, 1982. **21**(7): p. 1185-1190.

16. Zhu, Z., Y. Xu, and B. Jiang, *A One ppm NDIR Methane Gas Sensor with Single Frequency Filter Denoising Algorithm.* Sensors, 2012. **12**(9): p. 12729.

17. Fanchenko, S., et al. *LED-based NDIR natural gas analyzer*. in *IOP Conference Series: Materials Science and Engineering*. 2016. IOP Publishing.

18. Boudon, V., et al., *Spherical Top Theory and Molecular Spectra*, in *Handbook of High-resolution Spectroscopy*. 2011, John Wiley & Sons, Ltd.

19. Hecht, E. and A. Zając, *Optics*. 2nd ed. 1987, Reading, Mass.: Addison-Wesley Pub. Co. x, 676 p.

20. Novikov, V.A., *A filter*. 2001, Google Patents.

21. Capetanopoulos, C.D., *Controlled interference spectrometer*. 2006, Google Patents.

22. Valerie Alexey Novikov, d., *Filter*. 2007, Google Patents.

23. Tkachuk, M., *Optical absorption spectrometer and method for measuring concentration of a substance*. 2009, Google Patents.

24. A.N. Zaidel, G.V.O., Yu. I. Ostrovsky, *Tekhnika i praktika spektroskopii (Techniques and Practice of Spectroscopy) 2nd ed.* 1976, Moscow: Nauka.

25. Evans, J.V., *Monokhromaticheskie fil'try.* Solnechnaia sistema, 1957. **1**: p. 506-513.

26. Zirin, H., *Solnechnaia atmosfera*. 1969, Moscow.

27. Khromov, S., *Great Soviet Encyclopedia (a translation of the third edition).* Macmillan London, Collier Macmillan Publishers, 1978. **17**: p. 129.

28. Ward, T. and H. Zwick, *Gas cell correlation spectrometer: GASPEC.* Applied optics, 1975. **14**(12): p. 2896-2904.

29. Jones, E., T. Ward, and H. Zwick, *A fast response atmospheric CO 2 sensor for eddy correlation flux measurements.* Atmospheric Environment (1967), 1978. **12**(4): p. 845-851.

30. McCleese, D.J. and J.S. Margolis, *Remote sensing of stratospheric and mesospheric winds by gas correlation electrooptic phase-modulation spectroscopy.* Applied optics, 1983. **22**(17): p. 2528-2534.

31. Rider, D.M., et al., *Electrooptic phase modulation gas correlation spectroscopy: a laboratory demonstration.* Applied optics, 1986. **25**(17): p. 2860-2862.

32. Sachse, G.W. and L.-G. Wang, *Non-mechanical optical path switching and its application to dual beam spectroscopy including gas filter correlation radiometry*. 1992, Google Patents.

33. Drummond, J.R. *Measurements of pollution in the troposphere (MOPITT) instrument*. in *Optical Engineering and Photonics in Aerospace Sensing*. 1993. International Society for Optics and Photonics.

34. Sandsten, J., H. Edner, and S. Svanberg, *Gas imaging by infrared gas-correlation spectrometry.* Optics letters, 1996. **21**(23): p. 1945-1947.

35. Zhang, G.-h. and Y.-m. Wang. *Study of Jones Matrix of The Birefringent Crystal*. in *Photonics and Optoelectronics, 2009. SOPO 2009. Symposium on*. 2009.

36. Sellmeier, *Zur Erklärung der abnormen Farbenfolge im Spectrum einiger Substanzen.* Annalen der Physik, 1871. **219**(6): p. 272-282.

37. H. Rezig, M.N.a.A.B., *Study of Birefringent Spectral Filter for Photonic Systems.* Photonic Networks, Optical Technology and Infrastructure NOC '97. **1**: p. 299.

38. Bass, M., et al., *Handbook of Optics, Third Edition Volume II: Design, Fabrication and Testing, Sources and Detectors, Radiometry and Photometry*. 2010: McGraw-Hill, Inc. 1264.

39.   Almaz Optics, I. *Tellurium Dioxide (TeO2)*. 1993 [cited 2016; Available from: http://www.almazoptics.com/TeO2.htm.

40.   Fowles, G.R., *Introduction to Modern Optics*. 2012: Dover Publications.

41.   Priestley, R. *Birefringence dispersion in fused silica for DUV lithography*. 2001.

42.   Dally, J.W. and W.F. Riley, *Experimental stress analysis*. 1978: McGraw-Hill.

43.   Marlowe, M.O. and D. Wilder, *Elasticity and internal friction through the kilocycle range: reviwe and annotated bibliography.* 1964.

44.   Birger, E., *MDT demonstrates a new approach to quartz crystal microbalance design and application*, 685.jpg, Editor. 2010: http://www.nanotech-now.com/.

45.   Kemp, J.C., *Piezo-Optical Birefringence Modulators: New Use for a Long-Known Effect.* Journal of the Optical Society of America, 1969. **59**(8): p. 950-953.

46.   Statek-Techical-Note, *Statek Technical Note 32.*

47.   Gonzalez, G., *Foundations of Oscillator Circuit Design*. 2007: Artech House.

48.   Microchip Technology Inc., *20-Pin Flash-Based, 8-Bit CMOS Microcontroller with Two-Phase Asynchronous Feedback PWM Dual High-Speed Comparators and Dual Operational Amplifiers.* PIC16F785/HV785 Data Sheet, 2008.